Biophysical Journal
Article

Biophysical Society

Quantifying the Precision of Single-Molecule Torque and Twist Measurements Using Allan Variance

Maarten M. van Oene,[1] Seungkyu Ha,[1] Tessa Jager,[1] Mina Lee,[1] Francesco Pedaci,[1] Jan Lipfert,[1,2,*] and Nynke H. Dekker[1,*]

[1]Department of Bionanoscience, Kavli Institute of Nanoscience, Delft University of Technology, Delft, the Netherlands and [2]Department of Physics, Nanosystems Initiative Munich, and Center for Nanoscience, LMU Munich, Munich, Germany

ABSTRACT Single-molecule manipulation techniques have provided unprecedented insights into the structure, function, interactions, and mechanical properties of biological macromolecules. Recently, the single-molecule toolbox has been expanded by techniques that enable measurements of rotation and torque, such as the optical torque wrench (OTW) and several different implementations of magnetic (torque) tweezers. Although systematic analyses of the position and force precision of single-molecule techniques have attracted considerable attention, their angle and torque precision have been treated in much less detail. Here, we propose Allan deviation as a tool to systematically quantitate angle and torque precision in single-molecule measurements. We apply the Allan variance method to experimental data from our implementations of (electro)magnetic torque tweezers and an OTW and find that both approaches can achieve a torque precision better than 1 pN · nm. The OTW, capable of measuring torque on (sub)millisecond timescales, provides the best torque precision for measurement times $\lesssim$10 s, after which drift becomes a limiting factor. For longer measurement times, magnetic torque tweezers with their superior stability provide the best torque precision. Use of the Allan deviation enables critical assessments of the torque precision as a function of measurement time across different measurement modalities and provides a tool to optimize measurement protocols for a given instrument and application.

INTRODUCTION

Techniques to manipulate single-molecule have enabled studies of the structure, function, interactions, and mechanical properties of biological macromolecules at unprecedented detail (1–7). Many single-molecule manipulation techniques, notably optical tweezers and atomic force microscopy, naturally operate in the space of (linear) extension and force. However, biological macromolecules are frequently subject to torsional strain, and the molecular motors that translocate along them must be able to progress amid accumulated twist and torque. To quantify these phenomena, a number of techniques that enable measurements of rotation angle and torque (8,9) have been developed recently. Examples of such techniques (reviewed in (9)) include the rotor-bead-tracking assay (10–15), optical torque tweezers (16–28), and various extensions of magnetic tweezers comprising magnetic torque tweezers (29–32), freely orbiting magnetic tweezers (33,34), and electromagnetic torque tweezers (35). Similar to the field of force spectroscopy that has benefited from systematic analyses of the position and force precision of single-molecule techniques (36–44), torque- and twist-measuring techniques would be enriched by a better understanding of the achievable precision in angular detection and the determination of torque.

Here, we propose Allan deviation (AD) (38–49) as a criterion to systematically quantitate the angle and torque precision in single-molecule measurements. The AD allows us to critically assess the torque precision as a function of measurement time across different measurement modalities (e.g., magnetic versus optical torque tweezers) that rely on distinct physical principles. Being a real space quantity and having the same units as the observable of interest, it provides an intuitive and direct way to quantify and interpret precision (38–44). In addition to enabling direct quantitative comparisons of

Submitted October 2, 2017, and accepted for publication February 27, 2018.

*Correspondence: jan.lipfert@lmu.de or n.h.dekker@tudelft.nl

Maarten M. van Oene and Seungkyu Ha contributed equally to this work.

Mina Lee's present address is Center for Nano-Bio Measurement, Korea Research Institute of Standards and Science, Daejeon, Korea

Francesco Pedaci's present address is Department of Single-Molecule Biophysics, Centre de Biochimie Structurale, CNRS UMR 5048 UM INSERM U 1054, Montpellier, France

Editor: Thomas Perkins.

https://doi.org/10.1016/j.bpj.2018.02.039

different torque and twist measurement strategies, use of the AD in a systematic way provides an experimental user with a very convenient tool with which to optimize the measurement protocol for a given instrument and system. Here, we investigate the AD method using simulated traces and demonstrate its application to various implementations of magnetic torque tweezers (MTT), electromagnetic torque tweezers (eMTT), and an optical torque wrench (OTW). Using the AD analysis, we arrive at clear recommendations, e.g., for the optimal in-plane magnetic field strength in the eMTT and for choosing an optimal trapping laser power in the OTW.

MATERIALS AND METHODS

Definition and properties of AD

Given a time series of N observations of some quantity θ recorded at a sampling frequency f_s over a total measurement time $t_{meas} = N/f_s$, the Allan variance (AV) of θ for the time interval τ is defined as follows (42,43,45):

$$\sigma_\theta^2(\tau) = \frac{1}{2}\left\langle \left(\overline{\theta}_{i+1} - \overline{\theta}_i\right)^2 \right\rangle, \tag{1}$$

where $\overline{\theta}_i$ is the mean of the i^{th} measurement interval of length τ. The angle bracket $\langle \ldots \rangle$ denotes the arithmetic mean over all measurement intervals. In other words, the AV is one-half of the averaged square distance between the means of neighboring intervals. From its definition, the value of the AV is always greater than zero; it can only be computed for time intervals $\tau \leq t_{meas}/2$; it is additive for independent signals, i.e., the AV is the sum of the individual AVs; and it is linear, i.e., a linear scaling of θ, $\theta' = \alpha \cdot \theta$, will simply scale the AV as follows: $\sigma_{\theta'}^2(\tau) = \alpha^2 \cdot \sigma_\theta^2(\tau)$. The property of linearity is convenient because it allows for analysis of uncalibrated signals with the AV (e.g., one can analyze the voltage signal from a quadrant photodiode, position-sensing detector, or photodiode without having to first convert to position or torque units). In addition, the linearity enables simple conversion from angle to torque signal (by multiplication with the rotational trap stiffness, κ_θ, in units of pN · nm/rad) before or after evaluation of the AV. AD is defined as the square root of the AV: $\sigma_\theta(\tau) = (\sigma_\theta^2)^{1/2}$. Because AD has the same units as the quantity under investigation, it may be more intuitive to report ADs rather than AVs.

Computation of the AV

In practice, the AV is estimated from a data set with a finite number of measurements using a discrete form of Eq. 1. In the simple form of the AV, the data are split in M bins of m data points each, and the value of each bin is the mean over its m data points. The mean-square difference of consecutive bins estimates the AV:

$$\sigma_\theta^2(m\tau_s) = \frac{1}{2(M-1)} \sum_{i=1}^{M-1} \left(\overline{\theta}_{i+1} - \overline{\theta}_i\right)^2, \tag{2}$$

where τ_s is the sampling period and $\overline{\theta}_i$ is the mean of the i^{th} bin of length $m\tau_s$. The sampling period is taken to equal the integration time. For camera-based detection in the magnetic tweezers, this assumes no dead time between frames, which is justified given the typical dead time (~10 μs) relative to the integration time (~10 ms). For photodiode-based detection in the OTW, the situation is quite different; whereas the effective integration time is very fast (~10 ns), the photodiode is only read out at ~100 kHz. The inverse of this rate (~10 μs) is analogous to a dead time, as no signal averaging occurs. Thus, in the OTW, the dead time far exceeds the integration time. However, the application of Eq. 2 remains valid in all situations considered in this work because the sampling period is much shorter than the characteristic time of the system (Supporting Materials and Methods, Section 1). For each value of m, m frameshifts exist to compute the AV (Fig. 1 *A*). The use of all of these frameshifts improves the estimate of the AV and is known as the "overlapping" AV (Eq. S3 in Supporting Materials and Methods, Section 2).

Whereas the AV is defined for all values of m (up to the maximum $m = N/2$), the AVs for successive values of m are not independent and can be nearly identical because most values in a bin of size m are identical to the values in a bin of size $m+1$. For fitting of the AV data, it is therefore advantageous to calculate the octave-sampled AV by choosing $m = 2^{integer}$, which ensures nearly independent differences (46,47). We compute the AV (39) using a publicly available MATLAB (The MathWorks, Natick, MA) function (49). All AV curves are fit using maximum likelihood estimation with the shape factor by Lansdorp and Saleh (47) (Eq. S4 in Supporting Materials and Methods, Section 3).

Analytic expression for the AV of a Brownian particle in a harmonic trap

We employ the analytical expression given by Lansdorp and Saleh (47,48) for the AV of a particle undergoing Brownian motion in a harmonic well and apply it to the case of rotational motion, as follows:

$$\sigma_\theta^2 = A\left(\frac{\tau_c}{\tau}\right)^2 \left(2\frac{\tau}{\tau_c} + 4\exp\left(-\frac{\tau}{\tau_c}\right) - \exp\left(-2\frac{\tau}{\tau_c}\right) - 3\right), \tag{3}$$

where $A = k_BT/\kappa_\theta$ and $\tau_c = \gamma_\theta/\kappa_\theta$. Here, γ_θ is the rotational-friction coefficient and κ_θ is the trap stiffness of the rotational trap. Note that $k_BT/\kappa_\theta = Var(\theta)$ according to the equipartition theorem. We determine the friction coefficient γ_θ and the trap stiffness κ_θ by fitting the expression (Eq. 3) to our data using a maximum likelihood estimation algorithm (47). In the short time averaging limit, where diffusion is dominant, the AV reduces to the following:

$$\sigma_\theta^2 = \frac{2}{3}D\tau, \tag{4}$$

where D is the diffusion constant, which, according to the Einstein-Smoluchowski relation, equals k_BT/γ_θ.

In most single-molecule experiments, the short time regime provides little information about the system under study because the particle can barely respond to changes on these timescales, particularly for often relatively slow torque measurements. For long averaging times, the AV reaches the so-called thermal limit, where it reduces to the following:

$$\sigma_\theta^2 = 2A\frac{\tau_c}{\tau} = 2\frac{Var(\theta)}{n} = \frac{2k_BT\gamma_\theta}{\kappa_\theta^2\tau}, \tag{5}$$

where $n = \tau/\tau_c$ defines the number of independent observations. The averaging reduces the variance with the number of independent measurements n, and therefore, the AV decreases in a manner that is inversely proportional to τ, improving the angle precision. In between these two limits, the AV peaks at τ_{max}, with the best estimate of τ_{max} ($\approx 1.8926\tau_c$) coming from the numerical solution of Eq. 3 as opposed to the analytical solution ($= \sqrt{3}\,\tau_c$) of Eqs. 4 and 5.

Equations 3, 4, and 5 can be converted from angle to torque AV by straightforward application of the property of linearity; in the harmonic approximation, torque Γ is proportional to angle θ ($\Gamma = -\kappa_\theta \cdot \theta$), and hence, $\sigma_\Gamma^2 = \kappa_\theta^2 \cdot \sigma_\theta^2$. Thus, the thermal limit of the torque AV is given by the following:

$$\sigma_\Gamma^2 = \frac{2k_BT\gamma_\theta}{\tau}. \tag{6}$$

In this limit, the AV for torque is independent of the trap stiffness κ_θ, suggesting that stiffness has no effect on the torque precision in the regime in which the measurement precision is limited by thermal fluctuations (32).

Stochastic simulations of rotational motion

To test our AD analysis and to illustrate the effects of various system parameters, we simulate stochastic time traces of rotational motion using numerical solutions to the corresponding overdamped Langevin equation (Fig. 1). To simulate the rotation angle as a function of time $\theta(t)$, we discretize time into time steps Δt. The angle at time step $i+1$, θ_{i+1}, is given by the discretized overdamped Langevin equation as the following:

$$\theta_{i+1} = \theta_i + \left(\frac{\Gamma_{external} + \Gamma_{thermal}}{\gamma_\theta}\right)\Delta t, \qquad (7)$$

where the right-hand side only involves quantities known at time step i, γ_θ is the rotational friction coefficient (in units of pN · nm · s), $\Gamma_{external}$ is the external torque, and $\Gamma_{thermal} = N(0,1)\cdot(2k_BT\gamma_\theta/\Delta t)^{1/2}$ with thermal energy $k_BT \approx 4.1$ pN · nm at room temperature and with $N(0,1)$ being Gaussian-distributed noise with zero mean and unit SD. The Langevin dynamics simulations were implemented using custom MATLAB routines (Supporting Materials and Methods, Section 4).

AD measurements with magnetic tweezers

Torque application in magnetic tweezers relies on the alignment of superparamagnetic micron-sized beads or microspheres (referred to as "beads" from here on after) with an externally applied magnetic field (5,29,50). Both MTT and eMTT employ a predominantly vertical-oriented field generated by a cylindrical magnet and a smaller field in the horizontal direction generated by a side magnet in the MTT (32) (Fig. 2 *A*) or by electromagnets in the eMTT (35) (Fig. 3 *A*). The in-plane field generates a sufficiently weak angular trap to perform experiments on soft molecules, like DNA. Torque measurements in MTT and eMTT rely on tracking the rotational angle of the bead and observing changes in the equilibrium angle position of the bead inside the trap upon applying twist to a molecule of interest tethered between a surface and the magnetic bead. The torque is determined from the product of the angular shift and the trap stiffness, and hence, the angle AD can be determined directly from the angular traces, whereas the torque AD requires a calibrated trap stiffness. Limitations in angular tracking will therefore also affect the torque precision.

Our MTT and eMTT measurements of the AD use custom-built instruments described in detail elsewhere (32,35). In brief, they employ double-stranded DNA constructs bound to a flow cell surface via multiple digoxigenin-antidigoxigenin interactions and to superparamagnetic beads via multiple biotin-streptavidin interactions in phosphate-buffered saline. Bead sizes and DNA tether lengths are indicated in the main text and figure legends.

AD measurements with optical tweezers

The OTW is an extension of conventional optical tweezers that exploits the exchange of angular momentum between a nanofabricated, birefringent particle and a polarized trapping beam to apply and measure torque (16–28). Unlike the magnetic tweezers, which employ standard commercially available magnetic beads (whose magnetic anisotropy governs the achievable torque levels (50) and in which a choice of diameters permits control over the drag coefficient), for the OTW no comparable particles exist. Instead, one typically custom-fabricates birefringent dielectric particles using one of several fabrication routes (top-down, bottom-up, etc.), materials (quartz SiO_2 (0.009), vaterite $CaCO_3$ (0.1), calcite $CaCO_3$ (–0.16), rutile TiO_2 (0.26); optical birefringences specified in parentheses), shapes (spherical, cylindrical, etc.), and dimensions (with a size scale of a few micrometers being most prevalent) (23–28). In our custom-built instrument (22), we use cylindrically shaped rutile TiO_2 nanoparticles (diameter ~215 nm, height ~765 nm) fabricated in our cleanroom facility (26).

In the OTW, the optical tweezers trap a birefringent cylinder with its long axis aligned with the propagation direction of the light (Fig. 4 *A*). The linear polarization of the trapping laser clamps the angular position of the rutile TiO_2 cylinder, and rotation of this polarization controls rotation of the particle about its long axis (26). The imbalance between left and right circularly polarized components in the output of the trap provides a direct measure for the exchange of angular momentum inside the trap and, hence, a measure for the optical torque transferred to the particle. In the AD measurements, we fixed the direction of the linear polarization and measured the fluctuations around this equilibrium position (Figs. S8 *A* and S9 *A*). The power of the trapping laser is tuned using a half-wave plate and a polarizing beam splitter, in the range of 10–80 mW at the laser focus.

RESULTS

The AD is the square root of the AV, which is a type of variance that uses samples averaged over variable time intervals τ and that is computed from the difference between neighboring intervals (Materials and Methods). Although other approaches to quantifying precision exist (e.g., other variances, autocorrelation, or power spectrum analyses (Supporting Materials and Methods, Sections 5 and 6)), we find AD to be a particularly convenient measure for several reasons: 1) the AD at time τ provides a direct and intuitive measure of the precision expected for a measurement of a given duration; 2) being a real space quantity, the AD is immediately in the same units as that of the measured quantity of interest; 3) the AD is powerful in detecting low frequency, long-time scale drifts (43), which are critical for single-molecule measurements of torque and twist; and 4) the AD can be straightforwardly computed from the raw experimental data without the need to be calibrated a priori. In the following section, we explore the use of AD to quantify the angle and torque precision of single-molecule measurements. First, we present the results of stochastic simulations to introduce the concept of AD and validate our approach. We then use AD to compare the precision of three different single-molecule torque spectroscopy techniques: MTT, eMTT, and an OTW.

AD analysis of simulated traces

To explore the effects of the various system parameters on the AD, we simulated traces of the stochastic rotational motion of a bead subject to Brownian fluctuations while held in a harmonic trap (Fig. 1, *B–D*; Fig. S1). The simulated rotational motion (about an axis through the bead's center of mass) reveals the effects of varying rotational trap stiffness κ_θ and rotational drag coefficient γ_θ on the angular time trace (Fig. 1 *B*) and on the angle AD (Fig. 1 *C*) and torque AD (Fig. 1 *D*). In the green data set, $\gamma_\theta = 10$ pN · nm · s and $\kappa_\theta = 1000$ pN · nm/rad such that the characteristic time is $\tau_c = \gamma_\theta/\kappa_\theta = 10$ ms. To compare the effect of

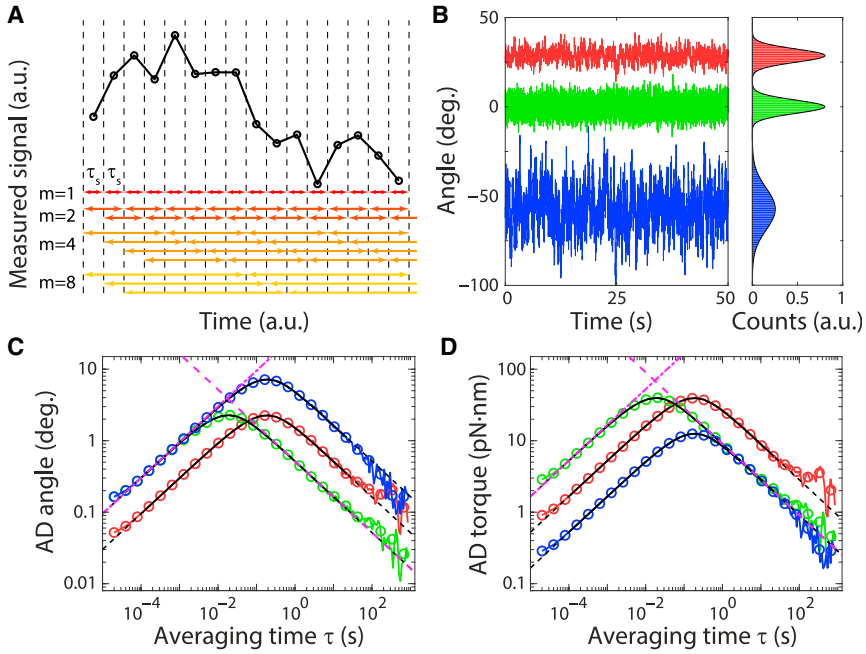

FIGURE 1 AD of simulated traces. (*A*) An illustration of the octave-sampled overlapping AD is shown. The example trace (*black*) contains 16 data points. Each data point is recorded during the sampling period τ_s. The data are split into bins of m data points. In octave-sampled data, $m = 2^{integer}$ (going from *red* to *yellow*, $m = 1$, 2, 4, 8). Splitting in bins is possible in m different frame shifts. For $m = 8$, only three frame shifts are displayed for clarity. (*B*) Simulated angle traces of ~1700 s each sampled at 50 kHz (corresponding to 8.5×10^7 data points) are shown for rotational Brownian motion of particles in harmonic traps. The left panel shows a zoom-in on the first 50 s of the traces, and the right panel shows the histograms for the full traces. The traces are offset vertically for clarity. The red, green, and blue traces (from top to bottom) are simulations with drag coefficient $\gamma_\theta = 100$, 10, and 10 pN · nm · s and trap stiffness $\kappa_\theta = 1000$, 1000, and 100 pN · nm/rad, respectively. (*C* and *D*) Angle and torque ADs for the traces in (*B*) are shown. Colored lines (*circles*) reflect the normal AD (octave-sampled overlapping AD). The results of the fits are indicated by solid black lines, and their extrapolations are indicated as dashed black lines (Eq. 3). The fitted parameters are $\gamma_\theta = 99.4 \pm 0.1$, 9.9 ± 0.01, and 10.0 ± 0.01 pN · nm · s and $\kappa_\theta = 1009.6 \pm 36.6$, 998.9 ± 9.7, and 99.6 ± 2.9 pN · nm/rad for the red, green, and blue data, respectively, from $N = 5$ independent simulated traces for each condition. The dash-dotted and dashed magenta lines are the diffusion and thermal limits, shown for the green data sets only. To see this figure in color, go online.

different drag coefficients, we simulate the red data set with the same stiffness but with a 10-fold-higher drag coefficient, $\gamma_\theta = 100$ pN · nm · s. To compare the effect of different stiffnesses, we generate the blue data set with the same drag coefficient as that of the green data set but with 10-fold-lower trap stiffness, $\kappa_\theta = 100$ pN · nm/rad. All other parameters are identical for the three simulated traces.

The simulated angle traces provide an instructive example of how the system parameters affect the observed behavior. The widths of the histograms (Fig. 1 *B*)—and thus, the amplitude of the angular fluctuations—are indifferent to changes in drag coefficient (compare *green* and *red* data sets) but are affected by changes in stiffness (compare *green* and *blue* data sets); a decrease in stiffness causes increased angular fluctuations, as expected from the equipartition theorem. Another feature visible in the angle traces is the timescale over which the angular fluctuations occur. The fluctuations in the green data appear "denser" on the time axis compared to the red and blue data because the characteristic time τ_c for the green data set (10 ms) is smaller than for the red and blue data sets (100 ms).

The ADs (Fig. 1, *C* and *D*) for our simulated traces all display the expected trend of an initial rise proportional to $\tau^{1/2}$ and a transition to a decrease proportional to $\tau^{-1/2}$ for larger τ (43). Changing the drag coefficient causes a shift of the curve on the time axis in both angle and torque ADs (*green* and *red* data sets). This shift indicates that a higher drag coefficient is linked to slower dynamics, which is consistent with the higher characteristic time τ_c. For the angle AD (Fig. 1 *C*), the change in stiffness initially has no effect; the curves overlap in the diffusion limit (*green* and *blue* data sets, Eq. 4). However, at longer timescales, a higher stiffness results in an improved angular precision (Eq. 5). In contrast, different stiffnesses do not alter the torque precision for large τ (Fig. 1 *D*) because in the thermal limit, the torque precision is independent of the trap stiffness κ_θ (Eq. 6). The analytical expression for the AV (Eq. 3) provides an excellent fit to the data, and we recover the values for κ_θ and γ_θ input into the simulations, confirming the validity of the method (Fig. 1, *C* and *D*, where the range of fitted data indicated by the black solid lines is constrained at the shortest and longest integration time limits to avoid the influence of noise not taken into consideration in Eq. 3); the same approach was followed in Figs. 2, 3, and 4.

Angle and torque precision in the MTT

The MTT employ a cylindrical magnet to generate a predominantly vertical-oriented field and a side magnet to apply an additional, smaller field in the horizontal direction. MTT measure torque by detecting changes in the equilibrium position of the bead-rotation angle about the tether axis upon over- and underwinding nucleic acid tethers (30–32) (Materials and Methods and Fig. S2, *A*–*C*). Here, we analyze traces of angular fluctuations recorded in our MTT implementation (Fig. 2 *A*) using a 2.8-μm-diameter magnetic bead and a 1-μm-diameter nonmagnetic fiducial

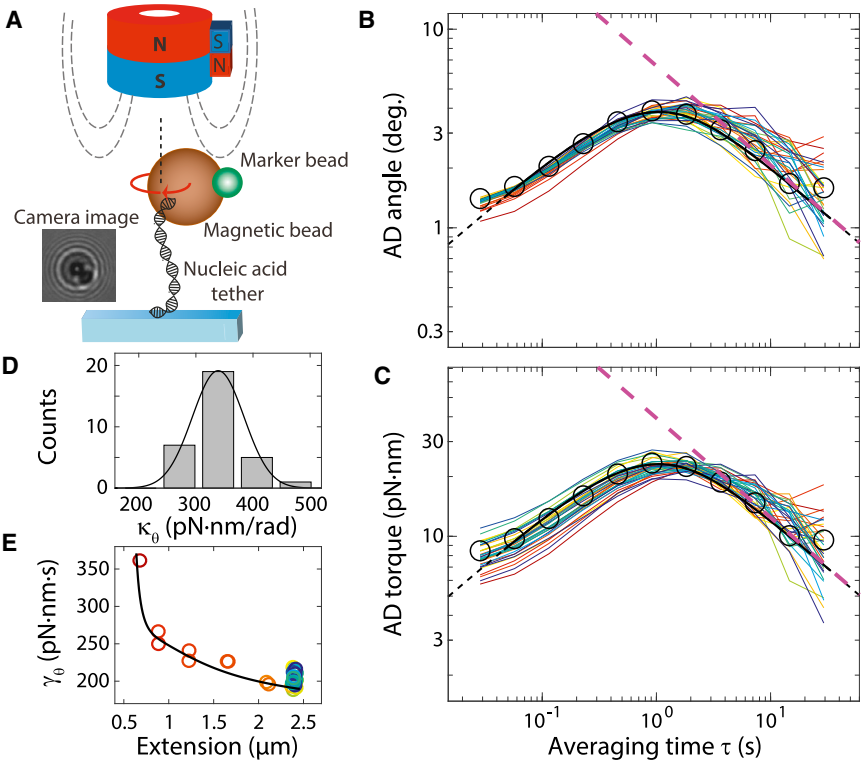

FIGURE 2 Angle and torque precision in the magnetic torque tweezers (MTT). (*A*) A schematic of the "classical" MTT implementation is shown (32). Angle tracking is achieved by attaching a smaller (1 μm diameter) nonmagnetic marker bead (*green*) to a larger (2.8 μm diameter) magnetic bead (*brown*) and tracking the rotation of the bead pair from charge-coupled device images (*inset*). The magnetic bead is tethered to a glass slide (*blue*) by a single DNA molecule (*black*), held, and manipulated in a weak rotational trap set up by vertically aligned permanent magnets with a side magnet added (*top*). The axis of bead rotation is indicated by the vertical dashed black line. (*B*) Octave-sampled overlapping ADs of 32 angle traces of 100 s each sampled at 35 Hz (corresponding to 3.5×10^3 data points) are shown, recorded in a torque measurement on a single 7.9 kbp DNA molecule (each trace is shown as a distinctly colored solid line, denoting the number of applied turns). The octave-sampled points for a single trace are shown as black circles. The fit of the analytical expression for the AV (Eq. 3) is shown as a solid black line, and its extrapolation is shown as a dashed black line. The thermal limit is indicated as a dashed magenta line. (*C*) Torque AD of the same traces as (*B*) obtained by multiplication with the corresponding trap stiffnesses (color-coding is as in (*B*)) is shown. Similar to (*B*), octave-sampled points for one trace are shown as black circles, the fit to Eq. 3 (multiplied by κ^2_θ) is shown as a solid black line, and its extrapolation is shown as a dashed black line. The thermal limit is indicated as a dashed magenta line. (*D*) The values for the trap stiffness κ_θ determined from the fits for all traces in (*B*) are shown. The data are approximately Gaussian distributed (*solid black line*) with a SD of 45 pN · nm/rad. (*E*) Rotational friction coefficients γ_θ (distinctly *colored circles*) determined from the AV fits for all traces in (*B*) are shown as a function of the height of the bead above the flow cell surface. The color-coding denotes the number of applied turns. The solid black line reflects a prediction for the rotational friction coefficient of a 2.8-μm-diameter bead rotating on a circular trajectory, taking into account corrections due to the presence of the surface. To see this figure in color, go online.

marker bead to track the rotation angle about the tether axis from analysis of camera images (51) (Fig. 2 *A*, *inset*). We focus on a representative data set consisting of 32 angle traces, recorded while over- and underwinding a 7.9 kbp DNA molecule tethered between the magnetic bead and the flow cell surface and held at a stretching force of ~2 pN. Upon over- and underwinding the DNA by integer numbers of turns, systematic changes of the equilibrium angle position are visible (Fig. S2 *C*, *middle panel*, *left axis*). These can be related to the changes in the torque exerted by the molecule (Fig. S2 *C*, *middle panel*, *right axis*) by multiplying with the mean trap stiffness (deduced from the fits to AD curves, as detailed below, and equivalent to deducing the trap stiffness from the SD of the angular fluctuations; Fig. S2 *C*, *top panel*). In addition, we observe that tether extension decreases rapidly past the buckling point of the DNA molecule for positive turns (corresponding to overwinding) but stays approximately constant for negative turns (corresponding to underwinding) because of torque-induced DNA melting (32,52) (Fig. S2 *C*, *bottom panel*).

Applying our AD analysis to the angle traces recorded in the MTT at different numbers of applied turns reveals some variability but indicates that we generally reach an angle precision of ~1° for a 50 s measurement (Fig. 2 *B*). From fits of the analytical expression (Eq. 3) to the angle AV data, we obtain the trap stiffness for each trace (Fig. 2 *D*), revealing a ~13% variation from trace to trace without any systematic changes throughout the measurement (Fig. S2 *D*). This yields a mean trap stiffness of 339 ± 45 pN · nm/rad, which is in excellent agreement with the value obtained from directly computing the SD of the angular fluctuations (330 ± 46 pN · nm/rad). Multiplying each angle AD curve by its fitted value of the trap stiffness, we convert the angle to a torque signal (Fig. 2 *C*). AD analysis of the torque signal indicates that the torque precision in the MTT follows the thermal limit (Fig. 2 *C*, *dashed magenta line*) for measurement times longer than ~2 s and reaches ~5 pN · nm after 50 s (Fig. 2 *C*). These results are consistent with our previous torque precision estimate for this setup (32) of 1–3 pN · nm for a 300 s measurement. In addition, we obtain values for the drag coefficient from the AV fits that exhibit systematic changes with DNA tether extensions, increasing by 70–80% upon decreasing the extension from 2.4 to 0.7 μm (Fig. 2 *E*). Both the observed value for the drag coefficients and the dependence on DNA extension are in reasonable agreement with the predictions

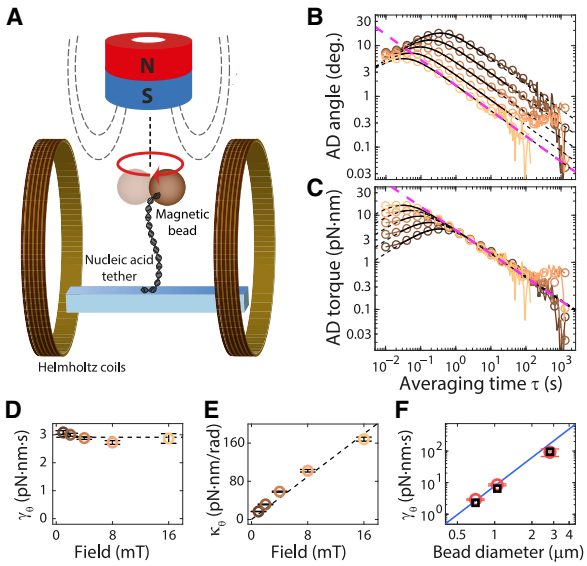

FIGURE 3 Angle and torque precision in the electromagnetic torque tweezers (eMTT). (*A*) A schematic of the eMTT setup (35) is shown. A magnetic bead (*brown*) is tethered to a glass slide (*blue*) by a single 3.4 kbp DNA molecule (*black*). The bead is lifted off from the surface by a cylindrical magnet (*top*). Four coils (only two are shown here) generate an in-plane magnetic field to orient the bead. Here, the angular orientation of the magnetic bead is deduced from its spatial position within a circular annulus whose radius is set by the distance between the tether attachment point and the pole of the magnetic bead (35). The axis of bead rotation is indicated by the vertical dashed black line. (*B*) The angle ADs of angle traces of ~2600 s each (except at 16 mT; 280 s) sampled at 100 Hz (corresponding to 2.6×10^5 data points) are shown, recorded on a single DNA-tethered bead at 1, 2, 4, 8, and 16 mT (going from *dark brown* to *light brown*). Colored lines (*circles*) reflect the normal AD (octave-sampled overlapping AD). The octave-sampled data are used to fit (*solid black lines*) the data to the analytical expression (Eq. 3), and their extrapolations are shown as dashed black lines. The dashed magenta line indicates the thermal limit for the stiffest trap. (*C*) The torque ADs of the same traces as (*B*) obtained by multiplication with the corresponding trap stiffnesses are shown. The color-coding is the same as in (*B*). The dashed magenta line indicates the thermal limit. (*D* and *E*) The values of the rotational drag coefficient γ_θ and the rotational trap stiffness κ_θ obtained from the fits in (*B*) are shown. The data points and their corresponding error bars denote the average and SD, respectively, from $N = 5$ independent measurements. In (*D*), the dashed black line is a constant-value fit to the drag coefficients. In (*E*), the dashed black line is a linear fit to the data through the origin. (*F*) Drag coefficients from AV fits for three different bead sizes ($d = 0.7$, 1.05, and 2.8 μm; Figs. S3–S5) are shown. Red circles and error bars are the drag coefficients (mean ± SD) determined from AV fits for differently sized beads (Figs. S3 *G*–S5 *G*) averaged over measurements at different field strengths. Black squares are the predictions from Eq. S10. The solid blue line is a fit of the scaling relation $\gamma_\theta \sim d^3$. To see this figure in color, go online.

of a model (Fig. 2 *E*, *solid black line*) that describes the rotation of a 2.8-μm-diameter bead along a circular trajectory, taking into account the increase in friction coefficient due to the proximity of the flow cell surface (53,54) (see Eq. S10 in Supporting Materials and Methods, Section 7). The observed dependence of the friction coefficient on DNA tether extension highlights the ability of our AD analysis to detect subtle changes in measurement parameters and demonstrates the importance of taking into account surface proximity effects when evaluating friction coefficients in single-molecule measurements (55).

Angle and torque precision in the eMTT at different fields

eMTT (Fig. 3 *A*) are similar to MTT; the main difference is that in the eMTT, electromagnets (implemented as two pairs of Helmholtz coils) generate a field in the horizontal direction. eMTT have an advantage over MTT in that the horizontal field component is readily tunable by altering the current in the Helmholtz coils (35). The ability to tune the trap stiffness, however, raises the question of what stiffness is optimal for a given torque measurement application. To explore the effects of trap stiffness and bead size, we measured angular fluctuations and analyzed the ADs of several differently sized DNA-tethered beads in the eMTT (Figs. S3–S5); for each bead size, measurements were carried out at different applied currents in the Helmholtz coils, corresponding to the different applied fields in the horizontal direction. We present the results of a single 0.7-μm-diameter bead trapped at different magnetic field strengths in Fig. 3.

From the AD of the angle signal in the eMTT, it is apparent that higher fields, corresponding to higher trap stiffnesses, give rise to a better angle precision (Fig. 3 *B*). For the 0.7-μm-diameter beads, the measurements reach ~1° precision in 3 s at the highest field strength of 16 mT (Fig. 3 *B*, *lightest brown*). This is much faster than what was observed in the MTT (~50 s, Fig. 2 *B*) despite the lower trap stiffness employed in the eMTT and results from our use of much smaller beads in the eMTT measurement. Converting the angle AD to torque AD by multiplication with the trap stiffness (itself deduced by fitting the corresponding angle AD curve), we find that the torque precision measurements are independent of trap stiffness in the thermal limit, i.e., at times longer than ~1 s (Fig. 3 *C*), as is expected from Eq. 6. The torque AD is identical for all employed trap stiffnesses for times between 1 and 100 s and already reaches a torque precision of ~5 pN · nm after 1 s, which is again much faster than in the MTT (~50 s, Fig. 2 *C*) because of the smaller beads used here. The torque precision reaches ~0.5 pN · nm for 100 s measurements (Fig. 3 *C*). The angle ADs are well described by the analytical expression in Eq. 3, yielding fitted drag coefficients γ_θ (Fig. 3 *D*) that are independent of the magnetic field, as expected, and fitted trap stiffnesses κ_θ (Fig. 3 *E*) that increase monotonically with the magnetic field. In the field range used in our implementation of the eMTT (1–16 mT), the dependence of κ_θ on field can be reasonably approximated as linear (35) (Fig. 3 *E*, *dashed black line*).

In these eMTT measurements, we start to see deviations from the thermal limit behavior ($\propto \tau^{-1/2}$) after ~100 s, and the torque AD signals for different field strengths begin

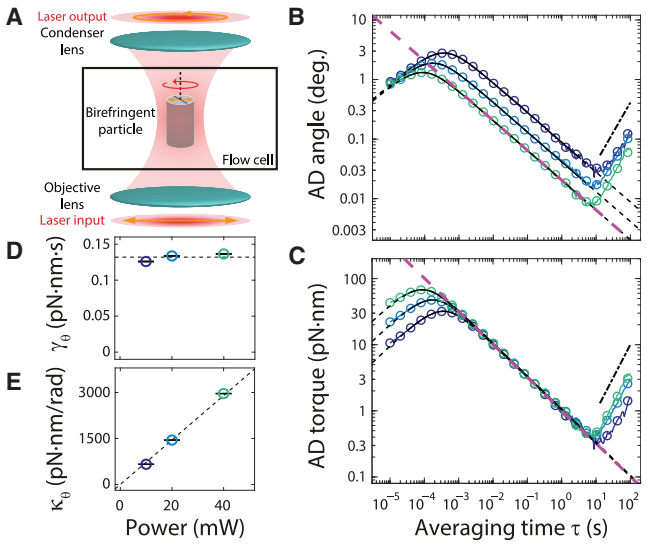

FIGURE 4 Angle and torque precision in the optical torque wrench (OTW). (*A*) A schematic of the OTW setup (22) is shown. The objective lens focuses a linearly polarized laser beam input (*red*) and traps a birefringent cylinder (*gray*) near the focus within a flow cell. Manipulation of the linear polarization allows us to control the angular position of the particle. At the output of the trap, the laser light is collected by a condenser lens. The polarization state of the output reports on the torque transferred from beam to particle. The axis of cylinder rotation is indicated by the vertical dashed black line. (*B*) The angle AD obtained from (*C*) by division with the corresponding trap stiffnesses is shown. Colored lines (*circles*) reflect the normal AD (octave-sampled overlapping AD). The color-coding is the same as in (*C*). The dashed magenta line indicates the thermal limit for the stiffest trap. (*C*) The torque ADs of torque traces of 200 s each sampled at 100 kHz (corresponding to 2.0×10^7 data points) are shown, recorded on a single rutile TiO_2 cylinder at 10, 20, and 40 mW (going from *dark blue* to *light green*). The octave-sampled data are used to fit (*solid black lines*) the data to the analytical expression (Eq. 3, multiplied by κ_θ^2), and their extrapolations are shown as dashed black lines. The fits only provide two independent parameters, γ_θ and κ_θ, so the system was precalibrated (22) to obtain the detector sensitivity in units of pN · nm/mV. The dashed magenta line indicates the thermal limit. The dash-dotted black line has slope of $+1$, corresponding to linear drift. (*D* and *E*) The values of the rotational drag coefficient γ_θ and the rotational trap stiffness κ_θ obtained from the fits in (*C*) are shown. The data points and their corresponding error bars denote the average and SD, respectively, from $N = 5$ independent measurements. In (*D*), the dashed black line is a constant-value fit to the drag coefficients. In (*E*), the dashed black line is a linear fit to the data through the origin. To see this figure in color, go online.

to differ. In general, for times longer than ~100 s, the torque AD is higher for higher field strengths because of pronounced drifts that become apparent with increases in the torque AD with time for long times (Fig. 3 *C*, see traces at 4 and 8 mT). The drifts are very likely due to heating of the coils when relatively high currents are run to achieve high fields for extended periods of time. Our present implementation of the eMTT requires ~16 A to achieve ~16 mT field and is air-cooled only (35). The heating is most dramatically visible in the trace at 16 mT, which had to be terminated after ~280 s (Fig. S3 *A*) as the coils reached a temperature of 60°C, at which point they are shut down by an automatic safety switch. A clear recommendation that emerges from the AD analysis is, therefore, to run at low field strengths (and thus low trap stiffnesses) in the eMTT for optimal torque measurements. In the absence of drift, higher trap stiffnesses do not confer any disadvantages in the torque precision; yet, the high currents required for high trap stiffnesses tend to cause significant drifts because of heating and thus deterioration of the torque precision for times longer than ~100 s. In contrast, for low currents and trap stiffnesses, we observe very low levels of drifts even for (very) long measurements, and reach, e.g., a best precision of ~0.1 pN · nm for ~1000 s measurements at ≤2 mT.

Angle and torque precision in the eMTT for different bead sizes

In addition, in the eMTT experiments, we probe the effect of different drag coefficients by comparing different bead sizes at a roughly constant trap stiffness (Fig. S6). Similar to the simulations (Fig. 1, *C* and *D*), a higher drag coefficient shifts the AD curve to longer timescales. At intermediate averaging times $\tau = 10$–100 s, the smaller the bead, the better the angle and torque precision, as expected from the corresponding thermal limits (Eqs. 5 and 6, respectively). The rotational drag coefficients obtained from the AV fits (Fig. 3 *F*, *red circles*) are in good agreement with predictions of the model (Fig. 3 *F*, *black squares*) that take into account the bead and tether geometry and surface effects (Eq. S10) and that roughly follow a $\gamma_\theta \sim d^3$ scaling, where d is the bead diameter (Fig. 3 *F*, *solid blue line*). The bead size analysis confirms that a decrease in drag coefficient improves the precision in both angle and torque.

As an independent test of the torque precision achieved in the eMTT, we analyzed a high-precision DNA torque measurement that employed 1.05-μm-diameter beads and a measurement time of 200 s per measurement point (Fig. S7 *A*). The torque AD analysis (Fig. S4 *F*) suggests that this measurement should achieve a torque precision of 0.5–0.9 pN · nm at ~200 s. We analyzed the deviations of the measured torque values from a strictly linear behavior in the elastic response regime (Fig. S7 *B*) and the deviations from constant torque in the DNA melting regime (Fig. S7 *C*). The deviations are approximately Gaussian distributed with SDs of 0.9 and 0.6 pN · nm for the two regimes, respectively, which is in excellent overall agreement with the expected precision from the AD analysis.

Angle and torque measurements in the OTW

In the OTW measurements, we keep the linear polarization of the trapping beam fixed and measure the torque transferred from the laser beam to a trapped, birefringent cylinder undergoing thermal fluctuations (Materials and Methods, Fig. 4 *A*). The cylinders are fabricated out of rutile TiO_2, which is selected over other materials (e.g., quartz SiO_2) for its extraordinarily high birefringence. Whereas

the OTW directly measures angular momentum transfer and thus torque, the torque traces are recorded in voltage. The corresponding AD can be converted to either the angle AD in degrees (Fig. 4 *B*) or the torque AD in pN · nm (Fig. 4 *C*) using parameters obtained through a separate calibration process (22). We also fit the torque AD (Eq. 3, multiplied by κ_θ^2) to obtain values for the parameters κ_θ and γ_θ. The drag coefficient γ_θ is nearly independent of laser power (Fig. 4 *D*) and averages to 0.13 ± 0.01 pN · nm · s, which is in good agreement with a theoretical value of ∼0.12 pN · nm · s (56). The angular trap stiffness κ_θ increases linearly with the laser power (Fig. 4 *E*), i.e., quadratically with the electric field amplitude (9). The ADs for the OTW data (Fig. 4, *B* and *C*) report on the precision of this experimental apparatus. As in the eMTT, we observe that angular precision improves, e.g., from ∼0.03° to ∼0.007° at ∼10 s (Fig. 4 *B*) with increased stiffness (achieved by increasing laser power from 10 to 40 mW). At the highest laser power, the measurements reach an angular precision of ∼1° after only 0.3 ms, which is a much shorter timescale than in the MTT and eMTT measurements, and it results from the higher trap stiffness and lower drag coefficient in the optical tweezers (compare *D* and *E* in Figs. 2, 3, and 4). For the torque AD (Fig. 4 *C*), all curves converge to the thermal limit. Similar dependencies for laser powers up to 80 mW were observed in a separate data set (Fig. S9).

The best torque precision in the OTW achieved is ∼0.3 pN · nm, which is comparable to ∼0.1 pN · nm precision achieved in the eMTT measurements. This requires the optimized environmental conditions reflected in Fig. 4 and Fig. S8 (see, for comparison, Fig. S9, where air currents induced earlier onset of drift) and is achieved after an averaging time of ∼10 s at a laser power of 10 mW (Fig. 4 *C*). On longer timescales, we find that drift in the OTW becomes dominant and deteriorates the precision. Similar dominance of drift only appears after ∼100 s in the eMTT and only at high Helmholtz fields (≥4 mT). The earlier onset of drift in the OTW compared to the eMTT derives from the increased number of optical and electronic components present, coupled to laser-power-dependent heating (observable from ∼10 s onwards in Fig. 4, *B* and *C*). These clear differences observed in the noise highlight the ability of our AD analysis to detect and compare noise components among different setups and environmental conditions.

DISCUSSION

Examination of the AD provides insights into the achievable precision and optimal measurement duration and parameters. For a hypothetical measurement without drift, the AD can become arbitrarily small, provided that the trace is averaged long enough, as the AD decreases in the thermal limit as $\tau^{-1/2}$. This would imply that the precision achievable experimentally could be arbitrarily high. In practice, of course, noise other than the white noise deriving from thermal fluctuations will kick in and limit further improvements in precision. Given the additive nature of the AD (Eq. 2), at a certain averaging time τ, drift will start to dominate over the thermal limit; on longer timescales, the precision will no longer improve with averaging but rather worsen. The resulting minimum in the AD then designates the best achievable precision and, hence, the optimum measurement time. Different sources of drift will exhibit distinct signatures in the AD. For example, for linear drift, the AD should increase as τ^1 (Supporting Materials and Methods, Section 6), as we observe for the OTW traces (Fig. 4, *B* and *C*, τ = 10–100 s). If the dominant source of noise has a $1/f$ character, then the AD scales as τ^0 (i.e., becomes constant; Supporting Materials and Methods, Section 6), as we observe around 2 s in the AD plots for the OTW data set presented in Fig. S9, *E* and *F*.

In this work, we have introduced the use of the AD to evaluate the performance of several instruments designed to measure torque on individual (biological) molecules. In both the MTT and eMTT measurements, drift does not appear to significantly limit the measurements, even for very long measurement times (Fig. 3, *B* and *C*, τ = 100–1000 s), provided that low enough Helmholtz fields (≤2 mT) are used to avoid drifts through heating of the coils in the eMTT configuration. It might be possible to avoid this limitation in future implementations, e.g., by configuring water-cooled coils. Nonetheless, even the current instrument enables measurements with a torque precision better than 1 pN · nm (Fig. 3 *C*; Figs. S3 *F*–S5 *F* and S7). We achieved a similar torque precision (∼0.3 pN · nm in 10 s, Fig. 4 *C*; for direct comparison with the eMTT, see Fig. S10) in the OTW under the best conditions (low laser power and blocking of air current). Potentially, the precision of the OTW can be enhanced by further improvements to the instrument's long-term stability.

A general lesson from our analysis is that to optimize torque and/or angle precision, the drag coefficient should be minimized particularly by using smaller particles (8). The eMTT data sets clearly demonstrate the improvements in precision obtained through using smaller beads; recent approaches to angle and torque measurements using gold nanoparticles push this development even further (15). Furthermore, once a particle size has been selected, it is generally advisable to maximize the trap stiffness for improved angle (but not torque) precision, given measurement times in which precision is thermally limited. However, there are important caveats to this general advice: first, smaller particles usually result in reduced stiffness and achievable torque because they contain less volume for torque exchange (lower magnetic content in magnetic beads and a shorter light path in birefringent particles); second, increasing the trap stiffness can result in increased drift because of practical limitations (e.g., heating from increased current in eMTT or laser power in OTW), deteriorating the precision for longer measurement timescales; third, the use

of ever-smaller particles may push the limits of the detection systems (e.g., pixel size for camera-based signal acquisition and diode sensitivity for photodiode-based signal acquisition); fourth, maximization of the trap stiffness and minimization of the drag coefficient reduce the characteristic time τ_c, which demands faster acquisition systems, as most calibration methods (and particularly AD analysis; see Supporting Materials and Methods, Section 1) require measurements on timescales shorter than τ_c; and finally, the timescale of dynamics in the system under investigation and the quantity of interest, angle or torque, ultimately determine the optimal drag coefficient and stiffness of operation.

The AD provides a direct and quantitative measure for the precision in single-molecule experiments. It can therefore be employed as a tool for optimizing experimental assays; it can be used to systematically track down sources of drift and other forms of noise and to determine the optimal measurement time at the desired precision. We foresee that usage of the AD analysis will instruct researchers about optimal measurement strategies and will thus facilitate new breakthroughs in the field of single-molecule torque spectroscopy.

SUPPORTING MATERIAL

Supporting Materials and Methods and eleven figures are available at http://www.biophysj.org/biophysj/supplemental/S0006-3495(18)30325-4.

AUTHOR CONTRIBUTIONS

M.M.v.O., J.L., and N.H.D. designed the research. J.L. and N.H.D. directed the research. T.J. and M.L. performed the MTT and eMTT experiments, respectively. M.M.v.O. and S.H. conducted the OTW experiments. M.M.v.O., S.H., and J.L. analyzed the data. All authors discussed the data and M.M.v.O., S.H., J.L., and N.H.D. wrote the manuscript.

ACKNOWLEDGMENTS

We thank Fabian Czerwinski for suggesting the use of AD for the analysis of torque spectroscopy experiments; Richard Janissen, Roland Kieffer, Margreet Docter, Jacob Kerssemakers, Sacha Khaiboulov, Dimitri de Roos, and Belen Solano Hermosilla for technical suggestions; Xander Janssen and Renier Daudey for performing preliminary eMTT measurements; and Roland Dries for assistance with the OTW setup.

This work is supported by funding provided by NanoNextNL, a micro- and nanotechnology consortium of the Government of the Netherlands and 130 partners (to N.H.D.); the Foundation for Fundamental Research on Matter (to N.H.D.); the Netherlands Organisation for Scientific Research (to N.H.D. and J.L.); the European Community's Seventh Framework Programme FP7/2007–2013 under grant agreement number 241548 (MitoSys; to N.H.D.); the European Research Council Consolidator grant (DynGenome) under grant number 312221 (to N.H.D.); and the German Research Foundation under grant number SFB 863 (to J.L.).

SUPPORTING CITATIONS

References (57–61) appear in the Supporting Material.

REFERENCES

1. Bustamante, C., Z. Bryant, and S. B. Smith. 2003. Ten years of tension: single-molecule DNA mechanics. *Nature.* 421:423–427.
2. Strick, T. R., M. N. Dessinges, …, V. Croquette. 2003. Stretching of macromolecules and proteins. *Rep. Prog. Phys.* 66:1–45.
3. Neuman, K. C., and A. Nagy. 2008. Single-molecule force spectroscopy: optical tweezers, magnetic tweezers and atomic force microscopy. *Nat. Methods.* 5:491–505.
4. Puchner, E. M., and H. E. Gaub. 2009. Force and function: probing proteins with AFM-based force spectroscopy. *Curr. Opin. Struct. Biol.* 19:605–614.
5. Vilfan, I. D., J. Lipfert, …, N. H. Dekker. 2009. Magnetic tweezers for single-molecule experiments. *In* Handbook of Single-Molecule Biophysics. P. Hinterdorfer and A. van Oijen, eds. Springer, pp. 371–395.
6. Dulin, D., J. Lipfert, …, N. H. Dekker. 2013. Studying genomic processes at the single-molecule level: introducing the tools and applications. *Nat. Rev. Genet.* 14:9–22.
7. Robinson, A., and A. M. van Oijen. 2013. Bacterial replication, transcription and translation: mechanistic insights from single-molecule biochemical studies. *Nat. Rev. Microbiol.* 11:303–315.
8. Bryant, Z., F. C. Oberstrass, and A. Basu. 2012. Recent developments in single-molecule DNA mechanics. *Curr. Opin. Struct. Biol.* 22:304–312.
9. Lipfert, J., M. M. van Oene, …, N. H. Dekker. 2015. Torque spectroscopy for the study of rotary motion in biological systems. *Chem. Rev.* 115:1449–1474.
10. Bryant, Z., M. D. Stone, …, C. Bustamante. 2003. Structural transitions and elasticity from torque measurements on DNA. *Nature.* 424:338–341.
11. Gore, J., Z. Bryant, …, C. Bustamante. 2006. Mechanochemical analysis of DNA gyrase using rotor bead tracking. *Nature.* 439:100–104.
12. Gore, J., Z. Bryant, …, C. Bustamante. 2006. DNA overwinds when stretched. *Nature.* 442:836–839.
13. Oberstrass, F. C., L. E. Fernandes, and Z. Bryant. 2012. Torque measurements reveal sequence-specific cooperative transitions in supercoiled DNA. *Proc. Natl. Acad. Sci. USA.* 109:6106–6111.
14. Oberstrass, F. C., L. E. Fernandes, …, Z. Bryant. 2013. Torque spectroscopy of DNA: base-pair stability, boundary effects, backbending, and breathing dynamics. *Phys. Rev. Lett.* 110:178103.
15. Lebel, P., A. Basu, …, Z. Bryant. 2014. Gold rotor bead tracking for high-speed measurements of DNA twist, torque and extension. *Nat. Methods.* 11:456–462.
16. Friese, M. E. J., T. A. Nieminen, …, H. Rubinsztein-Dunlop. 1998. Optical alignment and spinning of laser-trapped microscopic particles. *Nature.* 394:348–350.
17. Oroszi, L., P. Galajda, …, P. Ormos. 2006. Direct measurement of torque in an optical trap and its application to double-strand DNA. *Phys. Rev. Lett.* 97:058301.
18. La Porta, A., and M. D. Wang. 2004. Optical torque wrench: angular trapping, rotation, and torque detection of quartz microparticles. *Phys. Rev. Lett.* 92:190801.
19. Forth, S., C. Deufel, …, M. D. Wang. 2008. Abrupt buckling transition observed during the plectoneme formation of individual DNA molecules. *Phys. Rev. Lett.* 100:148301.
20. Inman, J., S. Forth, and M. D. Wang. 2010. Passive torque wrench and angular position detection using a single-beam optical trap. *Opt. Lett.* 35:2949–2951.
21. Pedaci, F., Z. X. Huang, …, N. H. Dekker. 2011. Excitable particles in an optical torque wrench. *Nat. Phys.* 7:259–264.
22. Pedaci, F., Z. Huang, …, N. H. Dekker. 2012. Calibration of the optical torque wrench. *Opt. Express.* 20:3787–3802.

23. Deufel, C., S. Forth, …, M. D. Wang. 2007. Nanofabricated quartz cylinders for angular trapping: DNA supercoiling torque detection. *Nat. Methods.* 4:223–225.
24. Gutiérrez-Medina, B., J. O. Andreasson, …, S. M. Block. 2010. An optical apparatus for rotation and trapping. *Methods Enzymol.* 475:377–404.
25. Huang, Z., F. Pedaci, …, N. H. Dekker. 2011. Electron beam fabrication of birefringent microcylinders. *ACS Nano.* 5:1418–1427.
26. Ha, S., R. Janissen, …, N. H. Dekker. 2016. Tunable top-down fabrication and functional surface coating of single-crystal titanium dioxide nanostructures and nanoparticles. *Nanoscale.* 8:10739–10748.
27. Parkin, S. J., R. Vogel, …, H. Rubinsztein-Dunlop. 2009. Highly birefringent vaterite microspheres: production, characterization and applications for optical micromanipulation. *Opt. Express.* 17:21944–21955.
28. Ramaiya, A., B. Roy, …, E. Schäffer. 2017. Kinesin rotates unidirectionally and generates torque while walking on microtubules. *Proc. Natl. Acad. Sci. USA.* 114:10894–10899.
29. Mosconi, F., J. F. Allemand, and V. Croquette. 2011. Soft magnetic tweezers: a proof of principle. *Rev. Sci. Instrum.* 82:034302.
30. Celedon, A., I. M. Nodelman, …, S. X. Sun. 2009. Magnetic tweezers measurement of single molecule torque. *Nano Lett.* 9:1720–1725.
31. Kauert, D. J., T. Kurth, …, R. Seidel. 2011. Direct mechanical measurements reveal the material properties of three-dimensional DNA origami. *Nano Lett.* 11:5558–5563.
32. Lipfert, J., J. W. J. Kerssemakers, …, N. H. Dekker. 2010. Magnetic torque tweezers: measuring torsional stiffness in DNA and RecA-DNA filaments. *Nat. Methods.* 7:977–980.
33. Lipfert, J., M. Wiggin, …, N. H. Dekker. 2011. Freely orbiting magnetic tweezers to directly monitor changes in the twist of nucleic acids. *Nat. Commun.* 2:439.
34. Lipfert, J., M. Wiggin, …, N. H. Dekker. 2015. Corrigendum: freely orbiting magnetic tweezers to directly monitor changes in the twist of nucleic acids. *Nat. Commun.* 6:7192.
35. Janssen, X. J., J. Lipfert, …, N. H. Dekker. 2012. Electromagnetic torque tweezers: a versatile approach for measurement of single-molecule twist and torque. *Nano Lett.* 12:3634–3639.
36. Moffitt, J. R., Y. R. Chemla, …, C. Bustamante. 2008. Recent advances in optical tweezers. *Annu. Rev. Biochem.* 77:205–228.
37. Capitanio, M., and F. S. Pavone. 2013. Interrogating biology with force: single molecule high-resolution measurements with optical tweezers. *Biophys. J.* 105:1293–1303.
38. Perkins, T. T. 2014. Ångström-precision optical traps and applications. *Annu. Rev. Biophys.* 43:279–302.
39. Andersson, M., F. Czerwinski, and L. B. Oddershede. 2011. Optimizing active and passive calibration of optical tweezers. *J. Opt.* 13:044020.
40. Huhle, A., D. Klaue, …, R. Seidel. 2015. Camera-based three-dimensional real-time particle tracking at kHz rates and Ångström accuracy. *Nat. Commun.* 6:5885.
41. Dulin, D., T. J. Cui, …, N. H. Dekker. 2015. High spatiotemporal-resolution magnetic tweezers: calibration and applications for DNA dynamics. *Biophys. J.* 109:2113–2125.
42. Gibson, G. M., J. Leach, …, M. J. Padgett. 2008. Measuring the accuracy of particle position and force in optical tweezers using high-speed video microscopy. *Opt. Express.* 16:14561–14570.
43. Czerwinski, F., A. C. Richardson, and L. B. Oddershede. 2009. Quantifying noise in optical tweezers by allan variance. *Opt. Express.* 17:13255–13269.
44. Mahamdeh, M., and E. Schäffer. 2009. Optical tweezers with millikelvin precision of temperature-controlled objectives and base-pair resolution. *Opt. Express.* 17:17190–17199.
45. Allan, D. W. 1966. Statistics of atomic frequency standards. *Proc. IEEE.* 54:221–230.
46. Allan, D. W., M. A. Weiss, and J. L. Jespersen. 1991. A frequency-domain view of time-domain characterization of clocks and time and frequency distribution systems. In Proceedings of the 45th Annual Symposium on Frequency Control (IEEE), pp. 667–678.
47. Lansdorp, B. M., and O. A. Saleh. 2012. Power spectrum and Allan variance methods for calibrating single-molecule video-tracking instruments. *Rev. Sci. Instrum.* 83:025115.
48. Lansdorp, B. M., and O. A. Saleh. 2014. Erratum: power spectrum and Allan variance methods for calibrating single-molecule video-tracking instruments. *Rev. Sci. Instrum.* 85:019901.
49. Czerwinski, F. 2010. Allan v3.0. In Matlab Central File Exchange. http://mathworks.com/matlabcentral/fileexchange/26659-allan-v3–0.
50. van Oene, M. M., L. E. Dickinson, …, N. H. Dekker. 2015. Biological magnetometry: torque on superparamagnetic beads in magnetic fields. *Phys. Rev. Lett.* 114:218301.
51. Lipfert, J., J. W. J. Kerssemakers, …, N. H. Dekker. 2011. A method to track rotational motion for use in single-molecule biophysics. *Rev. Sci. Instrum.* 82:103707.
52. Strick, T. R., V. Croquette, and D. Bensimon. 1998. Homologous pairing in stretched supercoiled DNA. *Proc. Natl. Acad. Sci. USA.* 95:10579–10583.
53. Leach, J., H. Mushfique, …, M. J. Padgett. 2009. Comparison of Faxén's correction for a microsphere translating or rotating near a surface. *Phys. Rev. E Stat. Nonlin. Soft Matter Phys.* 79:026301.
54. Faxen, H. 1922. Der Widerstand gegen die Bewegung einer starren Kugel in einer zähen Flüssigkeit, die zwischen zwei parallelen ebenen Wänden eingeschlossen ist. *Ann. Phys.* 68:89–119.
55. Lobo, S., C. Escauriaza, and A. Celedon. 2011. Measurement of surface effects on the rotational diffusion of a colloidal particle. *Langmuir.* 27:2142–2145.
56. Ortega, A., and J. García de la Torre. 2003. Hydrodynamic properties of rodlike and disklike particles in dilute solution. *J. Chem. Phys.* 119:9914–9919.
57. Howe, D. A., D. W. Allan, and J. A. Barnes. 1981. Properties of signal sources and measurement methods. In Proceedings of the 35th Annual Symposium on Frequency Control (IEEE), pp. A1–A47.
58. Volpe, G., S. Gigan, and G. Volpe. 2013. Simulation of a Brownian particle in an optical trap. *Am. J. Phys.* 81:224–230.
59. Rutman, J. 1978. Characterization of phase and frequency instabilities in precision frequency sources: fifteen years of progress. *Proc. IEEE.* 66:1048–1075.
60. Wong, W. P., and K. Halvorsen. 2006. The effect of integration time on fluctuation measurements: calibrating an optical trap in the presence of motion blur. *Opt. Express.* 14:12517–12531.
61. Yasuda, R., H. Miyata, and K. Kinosita, Jr. 1996. Direct measurement of the torsional rigidity of single actin filaments. *J. Mol. Biol.* 263:227–236.

Biophysical Journal, Volume *114*

Supplemental Information

Quantifying the Precision of Single-Molecule Torque and Twist Measurements Using Allan Variance

Maarten M. van Oene, Seungkyu Ha, Tessa Jager, Mina Lee, Francesco Pedaci, Jan Lipfert, and Nynke H. Dekker

Supplementary Text

S1. Comparison of magnetic tweezers and optical tweezers in applying Allan variance

The Allan variance is mathematically a two-sample variance with no dead time, where sampling interval T is the same as averaging time τ ($T = \tau$) (for details, see **Supplementary Text S5**):

$$\sigma_\theta^2(M, T, \tau) = \sigma_\theta^2(2, \tau, \tau) = \sigma_{AV,\theta}^2(\tau). \qquad \textbf{Equation S1}$$

For the magnetic tweezers (or other using video microscopy-based technique), there is negligible dead time between successive frames of a camera so that each measurement is a physical average of the signal during T ($T \approx \tau$), as described by the above equation. In the optical tweezers, detection occurs via photodiodes that have very fast response times. In this context, such a short response time can be considered as negligible integration time. Unless a specific configuration is employed in either acquisition hardware or software, no signal averaging (i.e., integration) occurs during the sampling interval T. Hence, the inverse of sampling frequency is equivalent to the dead time. Thus, in photodiodes the dead time far exceeds the integration time.

Nonetheless, the application of AV for photodiode-based detection remains valid provided that the sampling period T is much shorter than the characteristic time τ_c of the system. For such a case, a trapped particle essentially moves in a straight line between consecutive data points. For such a straight line, the average position calculated using the integral (corresponding to measurements that include averaging signal over T) is identical to the average of the two end points of the line (corresponding to measurements that consist of two sampled signal values without averaging over T). In other words, while optical tweezers measurements do not fulfill the zero-dead-time assumption ($T = \tau$) in a strict sense since physically $T \gg \tau$, effectively the measured signal is identical to that acquired over $T = \tau$ condition, provided that $T \ll \tau_c$. Hence, OTW and MT data can be interpreted with the same Allan variance equation. To our understanding, this forms the basis for the previous application of Allan variance analysis to linear optical tweezers data (e.g. Refs. (1-4)). The importance of fulfilling the condition $T \ll \tau_c$ in optical tweezers measurements is demonstrated in one of these literatures (Figure 4a of Ref. (1)), where it is shown that measured Allan variance curves show improved agreement with theoretical predictions when the data acquisition frequency f_s is sufficiently high ($T = f_s^{-1} \ll \tau_c$).

S2. The effect of noise correlation in Allan variance

The Allan variance is calculated from the difference between neighboring samples $\bar{\theta}_i$, which are averages over a time interval $m\tau_s$ (**Eq. 2** of the main text). For a single value of m, i.e., a single integration time, the differences are not all independent (**S2.1**). The number of independent differences is important, because it determines the noise on the Allan variance. Also, for different values of m, not all of the calculated Allan variance values are independent (**S2.2**). The independence of the Allan variance at different values of m is important, because it is a requirement in some fitting algorithms. Here, we elaborate on the independence between the difference terms of Allan variance, and discuss its implications for fitting Allan variance data.

S2.1. Independence of the difference between consecutive samples at a single integration time

For a data set with a finite number of elements, the "simple" Allan variance can be estimated from its discrete form (**Eq. 2** of the main text):

$$\sigma_\theta^2(m\tau_s) = \frac{1}{2(M-1)} \sum_{i=1}^{M-1} (\bar{\theta}_{i+1} - \bar{\theta}_i)^2 \,, \qquad \textbf{Equation S2}$$

where τ_s is the sampling period taken to be equal to the integration time (e.g., the dead time between frames is assumed to be zero in case of camera-based detection), m is the number of data points in a bin, M is the number of bins, and sample $\bar{\theta}_i$ is the mean of the i^{th} bin of length $m\tau_s$. The term $(\bar{\theta}_{i+1} - \bar{\theta}_i)$ will be referred to as the difference term. Each measurement $\bar{\theta}_i$, except for the first and last (i.e., $\bar{\theta}_1$ and $\bar{\theta}_M$), occurs twice in the difference term: once in conjunction with its preceding bin and once in conjunction with its successive bin. Therefore the $(M-1)$ difference terms are not all independent of each other (5).

The use of a fully "overlapping" Allan variance (**Fig. 1A**) can improve the estimate of the Allan variance even further:

$$\sigma_\theta^2(m\tau_s) = \frac{1}{2(N+1-2m)} \sum_{j=1}^{N+1-2m} \left(\bar{\theta}_{j+m} - \bar{\theta}_j\right)^2 \,, \qquad \textbf{Equation S3}$$

where $N = M \cdot m$ is the total number data points, j is the position of the first data point of a bin with m data points, and $\bar{\theta}_j$ is the average over a bin of length $m\tau_s$ with the first data point located at j. Here, the term $\left(\bar{\theta}_{j+m} - \bar{\theta}_j\right)$ will be referred to as the difference term. Again, each measurement $\bar{\theta}_j$ occurs twice, except for the first and last successive m measurements (i.e., $\bar{\theta}_1$, $\bar{\theta}_2$, $\bar{\theta}_3$, ... $\bar{\theta}_m$ and $\bar{\theta}_{N+1-2m+1}$, $\bar{\theta}_{N+1-2m+2}$, $\bar{\theta}_{N+1-2m+3}$, ... $\bar{\theta}_{N+1-2m+m}$). In addition, $\bar{\theta}_j$ also has overlapping data points with the successive $(m-1)$ measurements (i.e., $\bar{\theta}_{j+1}$, $\bar{\theta}_{j+2}$, $\bar{\theta}_{j+3}$, ... $\bar{\theta}_{j+(m-1)}$). Therefore the $(N+1-2m)$ difference terms are not all independent of each other.

The degree of dependence of the difference terms should be taken into consideration when computing the noise in the estimate of the Allan variance. In both the "simple" and "overlapping" Allan variance, the $(M-1)$ and $(N+1-2m)$ differences are normally distributed with zero mean (6), and the squared differences are gamma distributed, hence the estimate of the Allan variance is gamma distributed (6). The shape parameter of this gamma distribution is equal to half the number of degrees of freedom. Due to the aforementioned dependence of the difference terms, the number of degrees of freedom lies below the number of difference terms. It is important to know the number of degrees of freedom, as fitting algorithms such as maximum likelihood estimation account for the noise distribution of the calculated Allan variance, which involves the number of degrees of freedom. In their paper, Lansdorp and Saleh estimate the number of degrees of freedom and recommend a shape factor for the gamma distribution (**Supplementary Text S3**), which works reasonably well for fitting of both "simple" and "overlapping" Allan variances (6).

S2.2 Independence of the Allan variance at different integration times

Most fitting algorithms assume the noise of separate points, here the points at different integration times $m\tau_s$, to be independent. For different integration times, in particular for successive values of m, the Allan variances are calculated from different bin sizes; however, the difference terms of which the Allan variances are comprised can be nearly identical, because most values in a bin of size m are identical to the values in a bin of size $m+1$. Therefore calculating the Allan variance for all values of m is redundant; calculating the octave-sampled Allan variance for $m = 2^{integer}$ is sufficient and ensures nearly independent Allan variance values (7). Moreover, the octave-sampling has an advantage in computational efficiency over using all values of m. In our benchmark test, it is 108 ± 3, 852 ± 31, and 6620 ± 327 times shorter in computation time, for the input data sizes of 3×10^3, 3×10^4, and 3×10^5 elements (**Supplementary Fig. S11**). As an example, for 3×10^5 elements, only ~1 s was required to compute the octave-sampled AV while ~2 h was required when using all values of m. The benchmark test was repeated three times with a desktop PC equipped with Intel® Core™ i5-2400 (3.10 GHz) processor and 16 GBytes DDR3 (PC3-12800) memory.

S3. The shape factor used for MLE fitting of Allan variance data

The shape factor η_{AV} (**Eq. S4**) used in the maximum likelihood estimation (MLE) fitting of Allan variance data in our manuscript provides information about the extent to which the weighting is different between data points. We employ the following form:

$$\eta_{AV}(m) = \frac{1}{2}\left(\frac{N}{m} - 1\right), \qquad \textbf{Equation S4}$$

where N is the number of total data points and m is the bin size for the octave-sampled Allan variance, in powers of 2 (i.e., $m = 1, 2, 4, 8, \ldots$ up to $\leq N/2$) (6).

S4. Matlab routine for angular Langevin dynamics simulation

The Matlab code (tested in Matlab version R2017b) listed below is used to generate simulated angular fluctuation datasets in **Fig. 1** and **Supplementary Fig. S1**. It simulates a particle trapped in a harmonic potential while subject to overdamped angular motion (**Eq. 7** of the main text; also refer Equations S30-S32 of Ref. (8)). The equation of motion (and hence the Matlab code) are very similar to the case of linear trapping (Supplemental materials of Ref. (9)), except that the units of the physical quantities differ. After execution of this code, the `'theta'` array contains the angular position as a function of `'time'` array as shown in **Fig. 1B** and **Supplementary Fig. S1A**. This simulated raw data can be used to calculate Allan deviation and other plots such as ACF and PSD.

```
%%%%%%%%%%%%%   Angular Langevin dynamics simulation in Matlab   %%%%%%%%%%%%%

gamma = 10;                          % pN*nm*s, rotational drag coefficient
kappa = 1000;                        % pN*nm/rad, angular stiffness
kT = 4.1;                            % pN*nm, thermal energy at room temperature
dt = 20e-6;                          % s, sampling period
```

```
N = 2^20;                          % number of data points
Nloop = N - 1;                     % number of loops
time = (0:Nloop)*dt;               % s, time array
rv = randn([1,Nloop]);             % random variable (mean = 0, std = 1)
tau_thermal = rv*...
            sqrt(2*kT*gamma/dt);   % pN*nm, torque from thermal noise
theta(1) = 0;                      % rad, initial angular position
for i = 1:Nloop
 tau_external(i) = -kappa*theta(i); % pN*nm, external torque
 dtheta = ((tau_external(i) + ...
        tau_thermal(i))/gamma)*dt;  % rad, change in angular position
 theta(i+1) = theta(i) + dtheta;    % rad, angular position in the next step
end

%%%%%%%%%%%%%%%%%%%%%%%%%%%%%%%%%%%%%%%%%%%%%%%%%%%%%%%%%%%%%%%%%%%%%%%%%%%%%%
```

S5. Comparison of Allan variance to other variances

The Allan variance is a special case of the M-sample variance. This M-sample variance includes several other variances as special cases (including the commonly employed "normal" variance) and is expressed as (10):

$$\sigma_\theta^2(M,T,\tau) = \frac{1}{M-1}\sum_{i=1}^{M}\left(\bar{\theta}_i - \frac{1}{M}\sum_{j=1}^{M}\bar{\theta}_j\right)^2, \qquad \textbf{Equation S5}$$

where M is the number of samples, T is the time between samples, τ is the time over which each sample is averaged, $\bar{\theta}_i$ is the i^{th} measured sample averaged over τ, and $\frac{1}{M}\sum_{j=1}^{M}\bar{\theta}_j$ is the mean over all M samples. In most interpretations of the "normal" variance, the measurements are considered instantaneous ($\tau \to 0$, often $\tau \ll \tau_c$ is sufficient); the "normal" variance is $\sigma_\theta^2(M,T,0)$ or, written as an infinite time average, $\sigma_\theta^2 = \langle(\theta_i - \bar{\theta})^2\rangle$. For a white noise process, this variance is independent of the number of measurements M, so more measurements do not improve the precision of θ. If the time between measurements T equals the averaging time τ, the variance $\sigma_\theta^2(M,\tau,\tau)$ decreases for extended averaging time, thereby improving the precision. For example, the variance for Brownian motion in a harmonic potential is expressed as (11-13):

$$\sigma_\theta^2(M,\tau,\tau) = A\left(\frac{\tau_c}{\tau}\right)^2\left(2\frac{\tau}{\tau_c} + 2\exp\left(-\frac{\tau}{\tau_c}\right) - 2\right), \qquad \textbf{Equation S6}$$

where $A = k_BT/\kappa_\theta$ and $\tau_c = \gamma_\theta/\kappa_\theta$. This equation resembles the equation for the Allan variance (**Eq. 3** of the main text), and in the long time limit, $\tau \gg \tau_c$, it approaches the same thermal limit. In the short time limit, $\tau \ll \tau_c$, it converges to the "normal" variance, $\sigma_\theta^2 = k_BT/\kappa_\theta$. The minimum number of samples to calculate the M-sample variance is two, and the corresponding variance $\sigma_\theta^2(2,T,0)$ can be written as $\sigma_\theta^2(2,T,0) = \frac{1}{2}(\theta_2 - \theta_1)^2$ or, as an infinite time average, $\sigma_\theta^2 = \frac{1}{2}\langle(\theta_{i+1} - \theta_i)^2\rangle$. This variance uses the difference between neighboring measurements, instead of the difference from the mean. Therefore the two-sample variance is very useful in removing drift and other low frequency noise. The Allan variance is a two-sample variance with no dead time, i.e., $\sigma_{AV,\theta}^2(\tau) = \sigma_\theta^2(2,\tau,\tau)$ (10). The reduced sensitivity to drift at short time scales and the increase in precision (for white noise processes) at long time scales make the Allan variance a very useful tool in characterizing our single-molecule torque spectroscopy instruments.

S6. Comparison of Allan variance to power spectrum analysis

An alternative to the variances in the time domain is provided by the power spectral density in the frequency domain. The power spectrum describes to what extent different frequencies contribute to the variance. A power spectrum can be converted to the corresponding Allan variance using a transfer function $H(f)$ (10):

$$H(f) = \frac{2\sin^4(\pi\tau f)}{(\pi\tau f)^2}, \qquad \textbf{Equation S7}$$

$$\sigma_{AV}^2(\tau) = \int_0^\infty S(f)H(f)df\,, \qquad \textbf{Equation S8}$$

where $S(f)$ is the one-sided power spectrum. Conversely, the Allan variance $\sigma_{AV}^2(\tau)$ can be converted into a power spectrum $S(f)$ by plotting $2\tau\sigma_{AV}^2(\tau)$ as a function of $\pi\tau = f^{-1}$ (3). Some typical types of noise, like white noise, flicker noise, and Brownian noise are characterized by a frequency dependence with integer exponent, here f^0, f^{-1}, and f^{-2}, respectively. These three have corresponding time dependencies for the Allan variance, τ^{-1}, τ^0, and τ^1, respectively (10). As a remark, linear drift scales as τ^2, but the corresponding power spectrum does not scale as f^{-3} (10). The one-sided power spectrum for Brownian motion in a harmonic potential is given by:

$$S(f) = \frac{A}{1 + (f/f_c)^2}, \qquad \textbf{Equation S9}$$

where $A = 4\tau_c\, k_B T/\kappa$ and $f_c = \kappa/2\pi\gamma$. In the high frequency limit $f \gg f_c$, $S(f)$ is proportional to f^{-2}. This Brownian noise corresponds to the diffusion limit in the Allan variance $\propto \tau^1$ (**Eq. 4** of the main text). In the low frequency limit $f \ll f_c$, $S(f)$ is proportional to f^0. This white noise is linked to the thermal limit in the Allan variance $\propto \tau^{-1}$ (**Eq. 5** of the main text). If the frequency bandwidth $\Delta f \ll f_c$, the area under the power spectrum from 0 Hz to Δf approximates the angular precision by the variance $\sigma^2 = A \cdot \Delta f$ (14). The Allan variance, however, provides a much more convenient measure for the precision, especially if drift and low frequency noise become apparent.

S7. Rotational drag coefficient of a bead on a circular trajectory

A sphere of radius R_{bead}, rotating about an axis at a radial distance of R_{circle} from its center, at a distance D from the surface, immersed in a fluidic medium of viscosity η, has a rotational friction coefficient (Equation 18 of Refs. (15, 16)):

$$\gamma_\theta \approx \frac{\gamma_{rotational}}{1-\left(\frac{1}{8}\right)\left(\frac{R_{bead}}{D}\right)^3} + \frac{\gamma_{translational}R_{circle}^2}{1-\left(\frac{9}{16}\right)\left(\frac{R_{bead}}{D}\right)+\left(\frac{1}{8}\right)\left(\frac{R_{bead}}{D}\right)^3}, \qquad \textbf{Equation S10}$$

where $\gamma_{rotational} = 8\pi\eta R_{bead}^3$ and $\gamma_{translational} = 6\pi\eta R_{bead}$.

Supplementary Figures

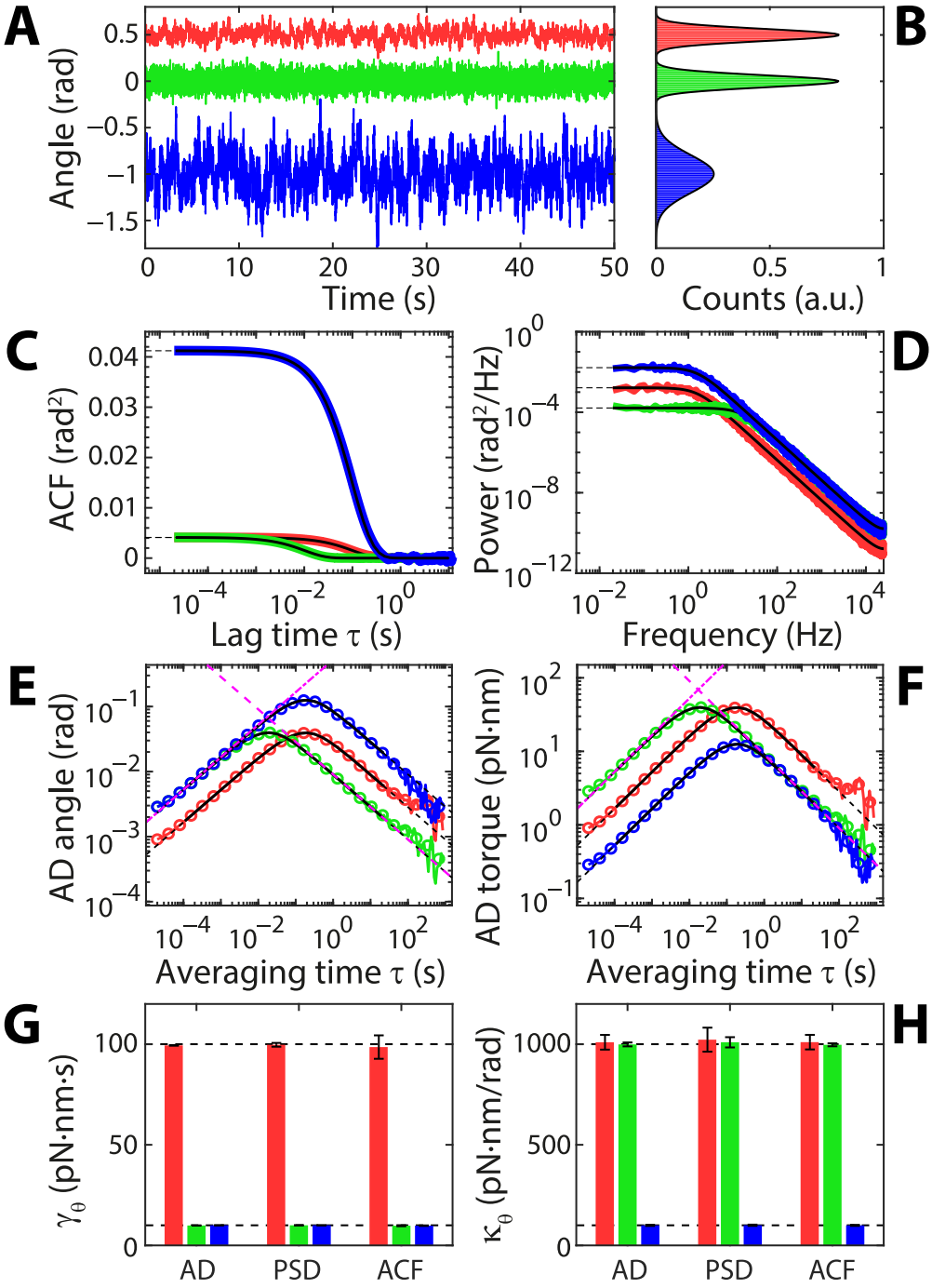

Figure S1. Additional analysis of the simulated traces in Fig. 1 of the main text. A) Simulated angle traces of ~1700 s each sampled at 50 kHz (corresponding to 8.5×10^7 data points) for the Brownian motion of a particle in a harmonic trap. A zoom-in on the first 50 s of each trace is shown. The traces are offset vertically for clarity. The red, green, and blue traces (from top to bottom) are simulations with drag coefficients γ_θ = 100, 10, and 10 pN·nm·s, and trap stiffnesses κ_θ = 1000, 1000, and 100 pN·nm/rad, respectively. Same data as in **Fig. 1B**. **B)** Histograms for the full traces. The solid black lines are Gaussian fits to the histograms. **C)** Autocorrelation function analysis (ACF) of the full traces. Black lines are fits to the data, $ACF \propto \exp(-\tau/\tau_c)$, with their extrapolations shown as dashed black lines. **D)** Power spectral density (PSD) analysis of the full traces. Black lines are fits to the data (**Eq. S9**). **E)** Angle Allan deviation (AD). Colored lines (circles) reflect the normal AD (octave-sampled overlapping AD). Same data as in **Fig. 1C**. The solid black lines are fits to the data (**Eq. 3**). The dash-dotted and dashed magenta lines are the diffusion and thermal limits, shown for the green trace only. **F)** Torque AD. Same data as in **Fig. 1D**. **G,H)** Rotational drag coefficient γ_θ and trap stiffness κ_θ obtained from the AD, PSD, and ACF fits. The bar heights and error bars denote the average and standard deviation, respectively, from N = 5 independent simulated traces. The dashed black lines indicate the parameter values used in the simulations.

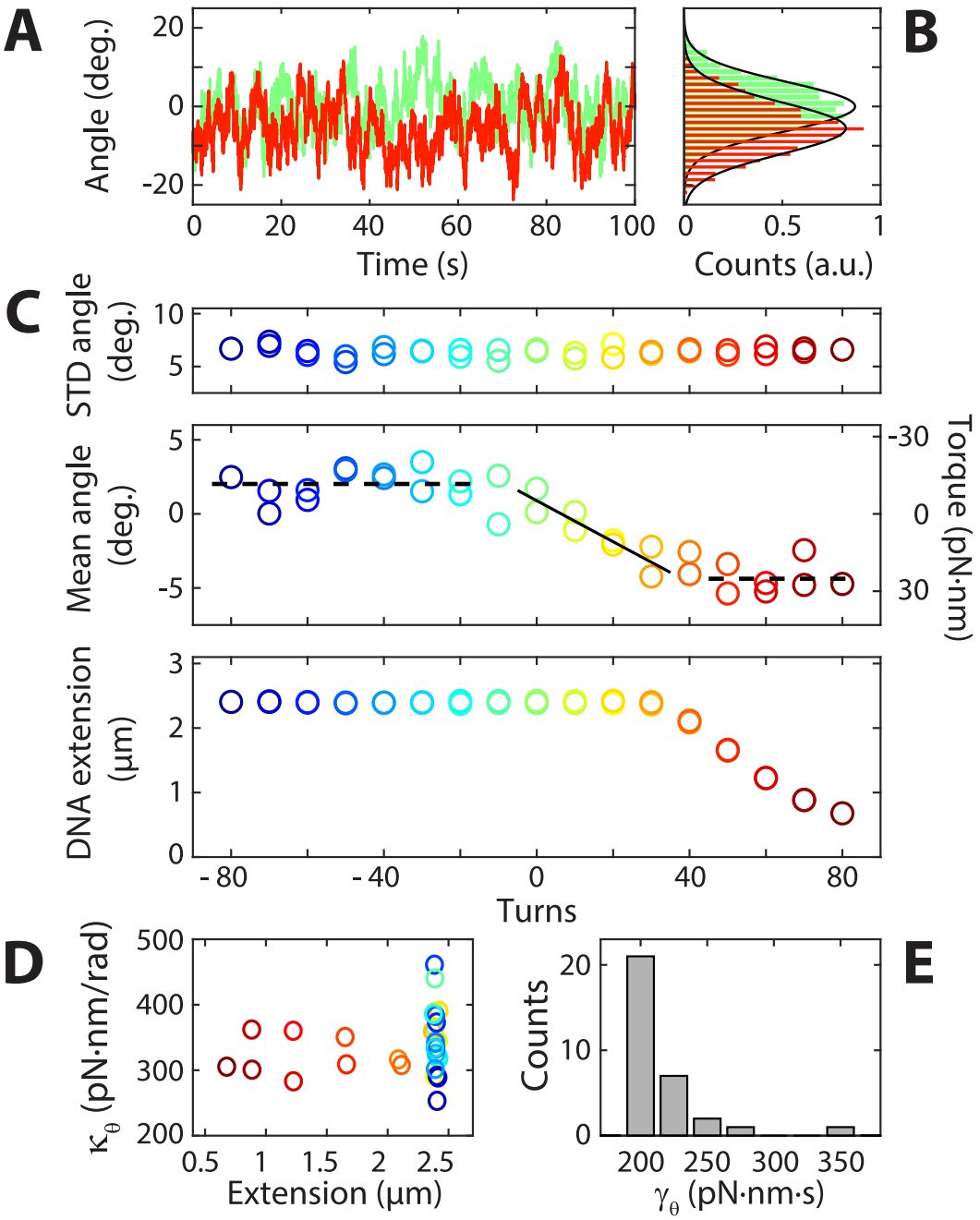

Figure S2. Torque measurements in the MTT. Data shown are for a 2.8 μm diameter magnetic bead tethered to a surface by a 7.9 kbp DNA molecule at a stretching force of ~2 pN in PBS buffer, using the same data as in **Fig. 2** of the main text. **A)** Angle traces of 100 s each at 0 (light green) and 50 turns (red). **B)** Histograms of the full traces. The solid black lines are Gaussian fits to the histograms. A shift in the mean angle position upon overwinding the molecule is readily apparent and provides the basis for the single-molecule torque measurement. **C)** Systematic analysis of angle traces as a function of the number of applied turns, such as the ones shown in **A**,**B)**, reveals systematic shifts in the mean angle (middle panel), while the standard deviations of the fluctuations remain constant (top panel). The data points are color-coded as a function of the number of applied turns. The average trap stiffness (~339 pN·nm/rad) of the rotational trap is determined from Allan variance fits, enabling a direct conversion of the mean angle to torque (middle panel, right axis). The bottom panel shows the tether extension as a function of the applied number of turns obtained in the same measurement. The tether extension decreases linearly with the number of applied turns beyond ~35 turns, as the molecule buckles and is plectonemically supercoiled in this regime. Note the corresponding plateau in the torque signal (~24 pN·nm) for > 35 turns (the dashed black line in this regime is a constant-value fit). Around zero turns, the molecule opposed the applied torque elastically, resulting in an approximately constant extension of the molecule and a linear dependence of the torque on applied turns (the solid black line in this regime is a linear fit). Upon underwinding (corresponding to negative turns), the DNA extension remains approximately constant and the torque exhibits a plateau at the critical melting torque ~–11 pN·nm (the dashed black line in this regime is a constant-value fit). **D)** Trap stiffness determined from Allan variance fits (same data as in **Fig. 2D**), shown as a function of DNA extension. Color-coding is as in **C)**. **E)** Histogram of the friction coefficient determined from the Allan variance fits (same data as in **Fig. 2E**).

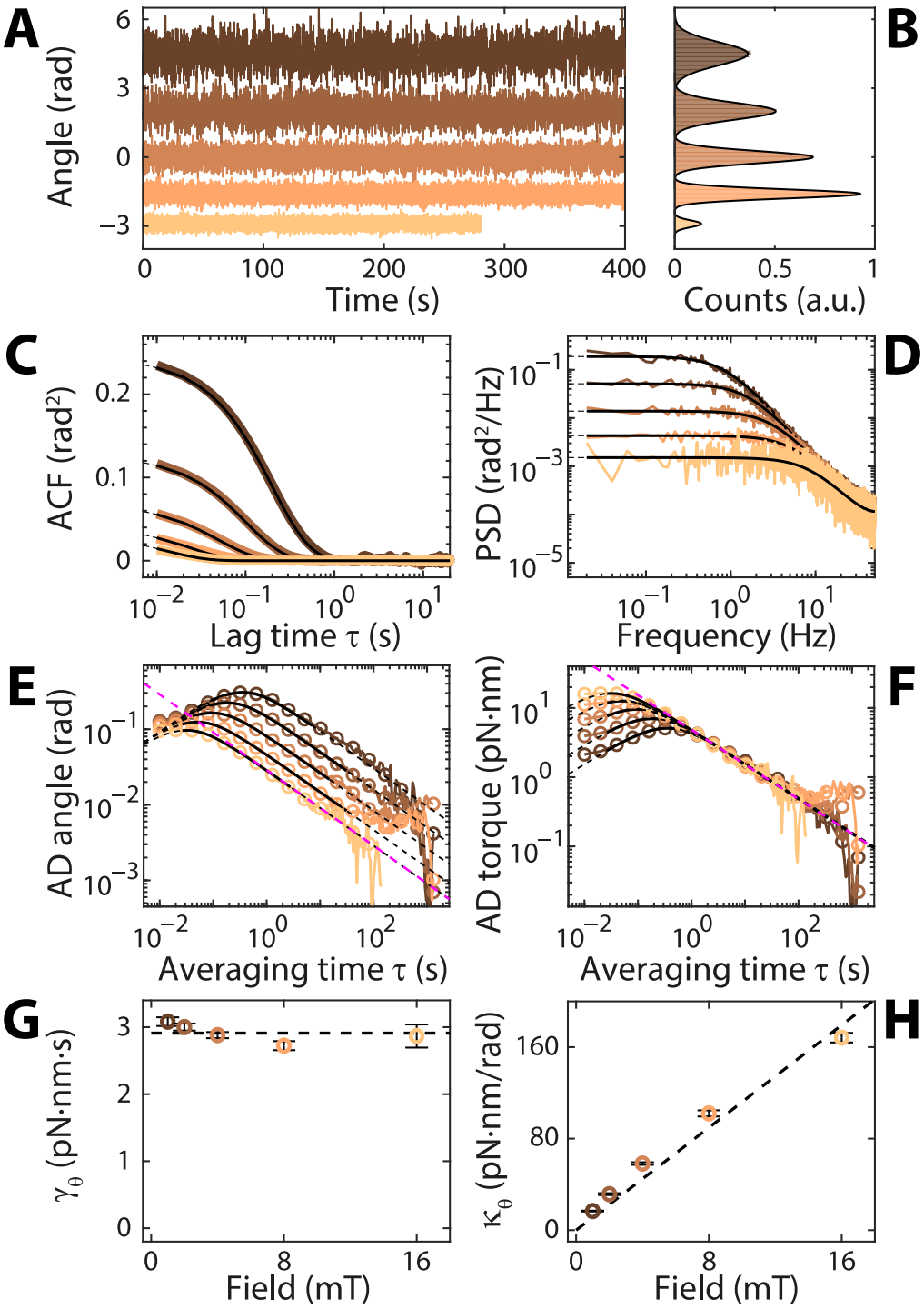

Figure S3. Additional analysis of the eMTT data for 0.7 µm diameter beads. Data and color-coding (increasing magnetic field strengths of 1, 2, 4, 8, and 16 mT, going from dark brown to light brown) as in **Fig. 3** of the main text. **A)** Zoom-in on the first 400 s (at 16 mT, 280 s) of the angle traces of ~2600 s each sampled at 100 Hz (corresponding to 2.6×10^5 data points). The traces are offset vertically for clarity. **B)** Histograms over the full traces. The solid black lines are Gaussian fits to the histograms. **C)** Autocorrelation function analysis. The solid black lines are fits to the data, and their extrapolations are shown as dashed black lines. **D)** Power spectrum analysis. **E)** Angle Allan deviation (AD). Colored lines (circles) reflect the normal AD (octave-sampled overlapping AD). Same data as in **Fig. 3B**. The dashed magenta line indicates the thermal limit for the stiffest trap. The fitted parameters are displayed in **G,H)**. **F)** Torque AD. Same data as in **Fig. 3C**. The dashed magenta line corresponds to the thermal limit. **G)** Rotational drag coefficient γ_θ obtained from the AD fits in **E)** versus magnetic field strength. The dashed black line is a constant-value fit to the data. Same data as in **Fig. 3D**. The data points and their corresponding error bars denote the average and standard deviation, respectively, from $N = 5$ independent measurements. **H)** Rotational trap stiffness κ_θ obtained from the AD fits in **E)** versus magnetic field strength. The solid black line is a linear fit to the data. Same data as in **Fig. 3E**.

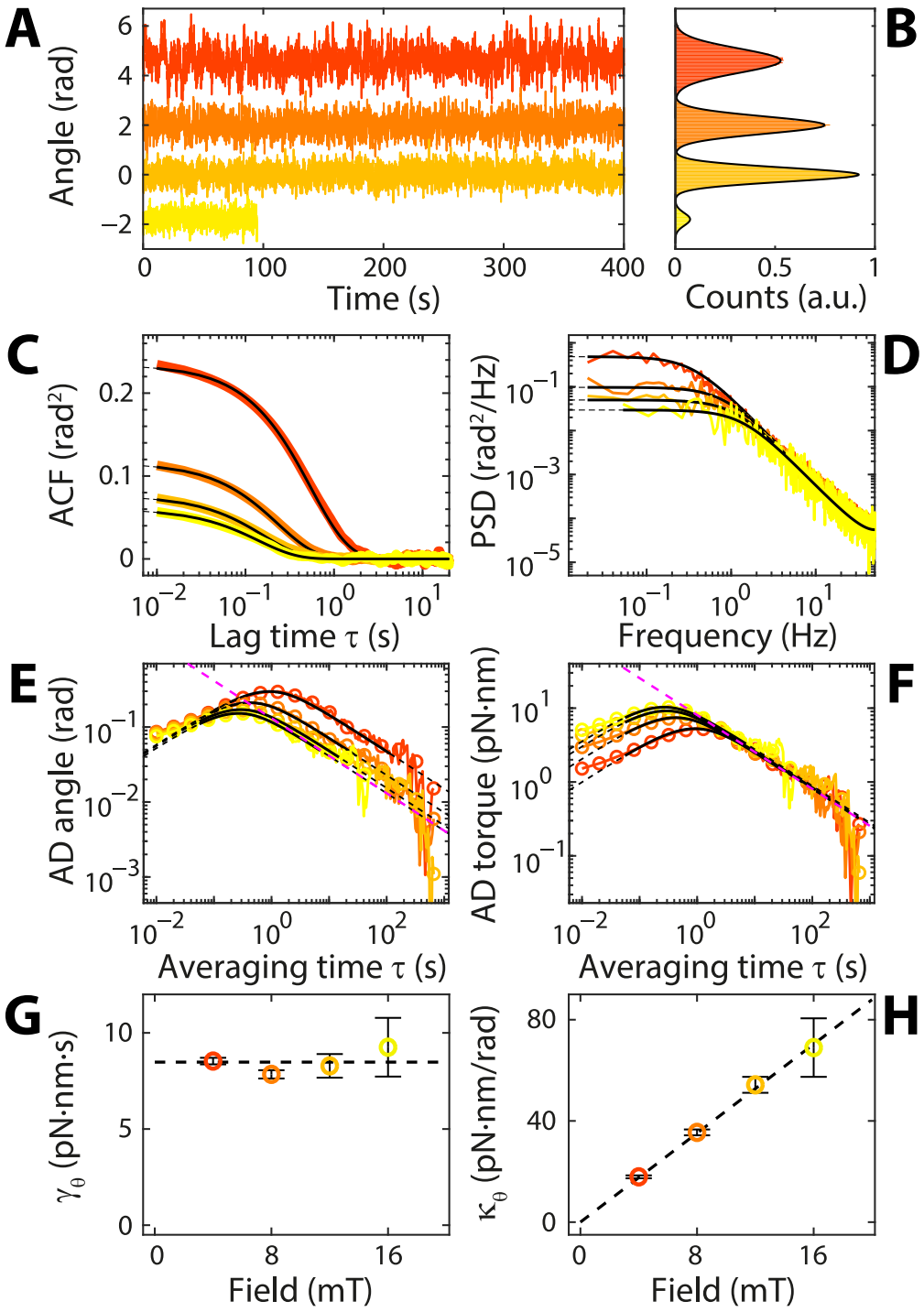

Figure S4. MyOne (1.05 µm diameter) beads trapped at different field strengths using eMTT. The color-coding indicates increasing magnetic field strength (4, 8, 12, and 16 mT, going from red to yellow). **A)** Zoom-in on the first 400 s (at 16 mT, 95 s) of the angle traces of ~1300 s each sampled at 100 Hz (corresponding to 1.3×10^5 data points). The traces are offset vertically for clarity. **B)** Histograms over the full traces. The solid black lines are Gaussian fits to the histograms. **C)** Autocorrelation function analysis. The solid black lines are fits to the data, and their extrapolations are shown as dashed black lines. **D)** Power spectrum analysis. **E)** Angle Allan deviation (AD). Colored lines (circles) reflect the normal AD (octave-sampled overlapping AD). The dashed magenta line indicates the thermal limit for the stiffest trap. The fitted parameters are displayed in **G,H)**. **F)** Torque AD. The dashed magenta line corresponds to the thermal limit. **G)** Rotational drag coefficient γ_θ obtained from the AD fits in **E)** versus magnetic field strength. The dashed black line is a constant-value fit to the data. The data points and their corresponding error bars denote the average and standard deviation, respectively, from $N = 5$ independent measurements. **H)** Rotational trap stiffness κ_θ obtained from the AD fits in **E)** versus magnetic field strength. The dashed black line is a linear fit to the data.

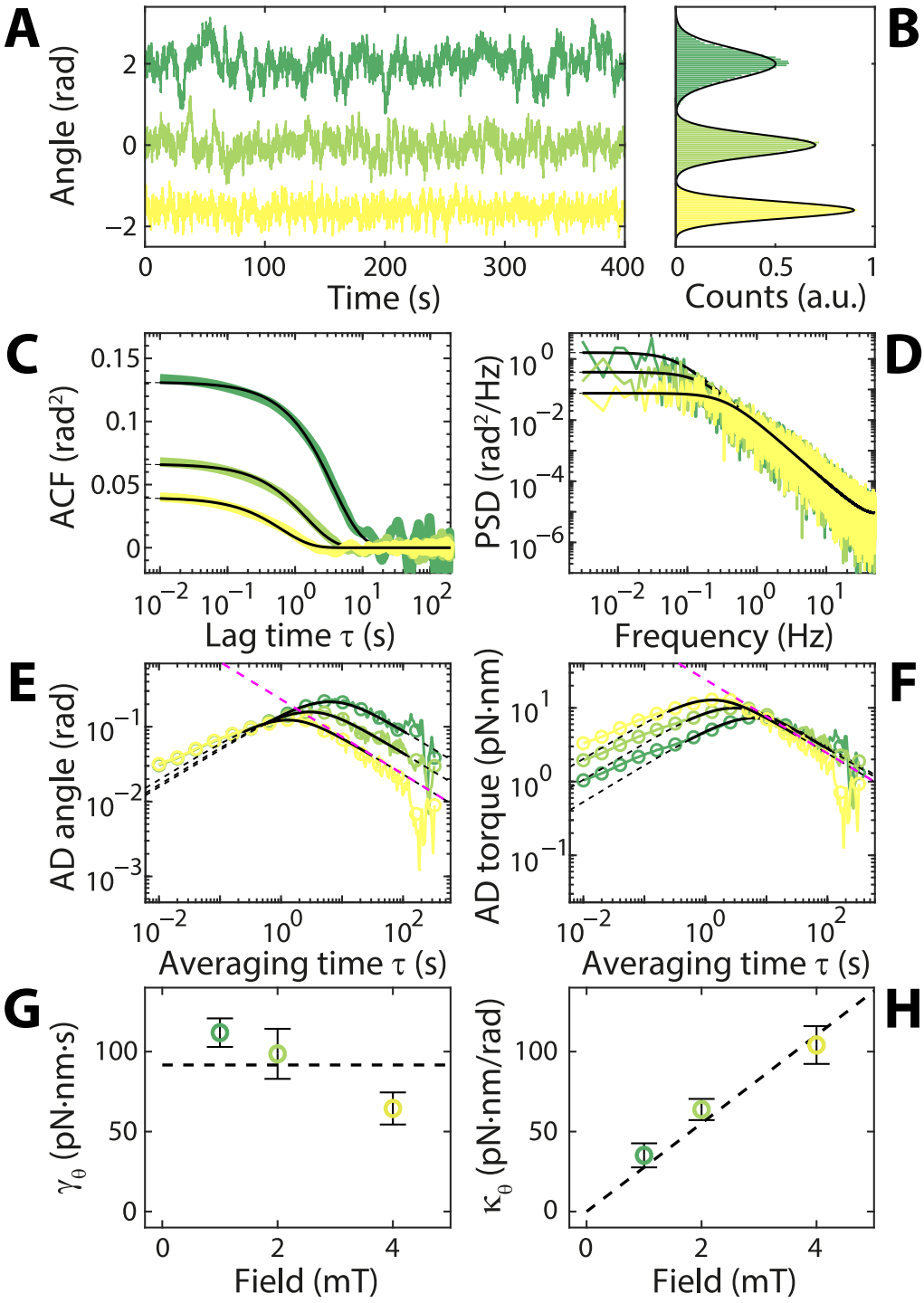

Figure S5. M270 (2.8 µm diameter) beads trapped at different field strengths using eMTT. The color-coding indicates increasing magnetic field strength (1, 2, and 4 mT, going from green to light yellow). **A)** Zoom-in on the first 400 s of the angle traces of ~650 s each sampled at 100 Hz (corresponding to 6.5×10^4 data points). The traces are offset vertically for clarity. **B)** Histograms over the full traces. The solid black lines are Gaussian fits to the histograms. **C)** Autocorrelation function analysis. The solid black lines are fits to the data, and their extrapolations are shown as dashed black lines. **D)** Power spectrum analysis. **E)** Angle Allan deviation (AD). Colored lines (circles) reflect the normal AD (octave-sampled overlapping AD). The dashed magenta line indicates the thermal limit for the stiffest trap. The fitted parameters are displayed in **G,H)**. **F)** Torque AD. The dashed magenta line corresponds to the thermal limit. **G)** Rotational drag coefficient γ_θ obtained from the AD fits in **E)** versus magnetic field strength. The dashed black line is a constant-value fit to the data. The data points and their corresponding error bars denote the average and standard deviation, respectively, from $N = 3$ independent measurements. **H)** Rotational trap stiffness κ_θ obtained from the AD fits in **E)** versus magnetic field strength. The dashed black line is a linear fit to the data.

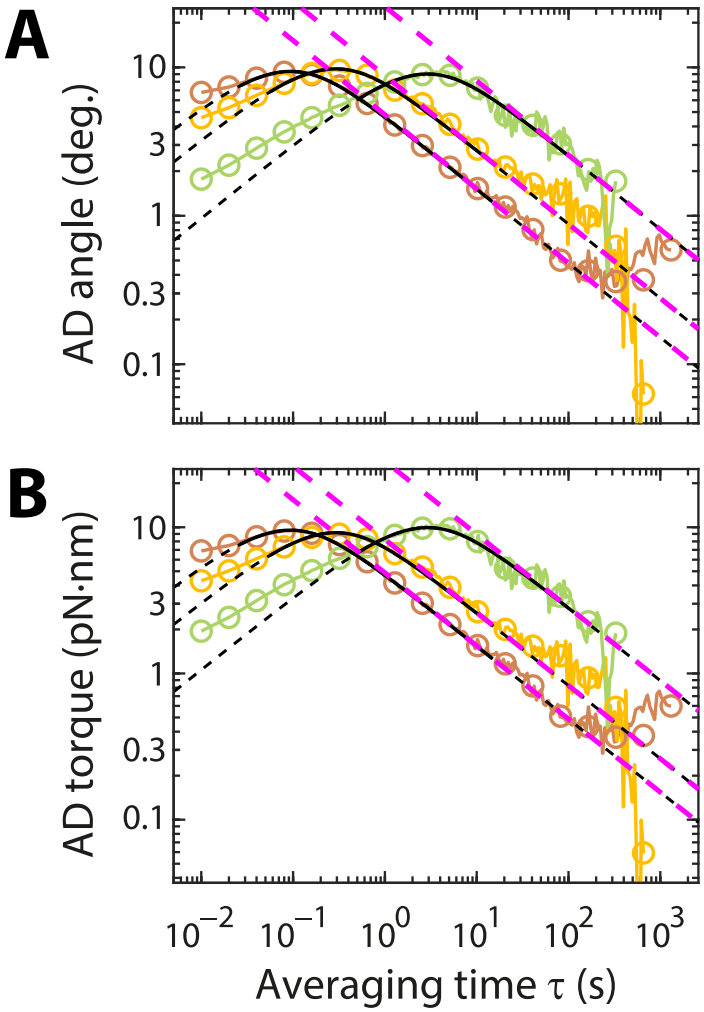

Figure S6. Angle and torque Allan deviation for different bead sizes in the eMTT. The traces were selected from **Supplementary Figs. S3-S5** in order to obtain similar trap stiffnesses (~60 pN·nm/rad). We record the fluctuations of a MagSense bead ($d = 0.7$ µm) at 4 mT (brown, $\kappa_\theta = 58$ pN·nm/rad), a MyOne bead ($d = 1.05$ µm) at 12 mT (orange, $\kappa_\theta = 54$ pN·nm/rad), and a M270 bead ($d = 2.8$ µm) at 2 mT (light green, $\kappa_\theta = 64$ pN·nm/rad). **A)** Angle Allan deviation. **B)** Torque Allan deviation. The solid black lines are fits to the data, and their extrapolations are shown as dashed black lines in **A,B)**. The dashed magenta lines indicate the thermal limits.

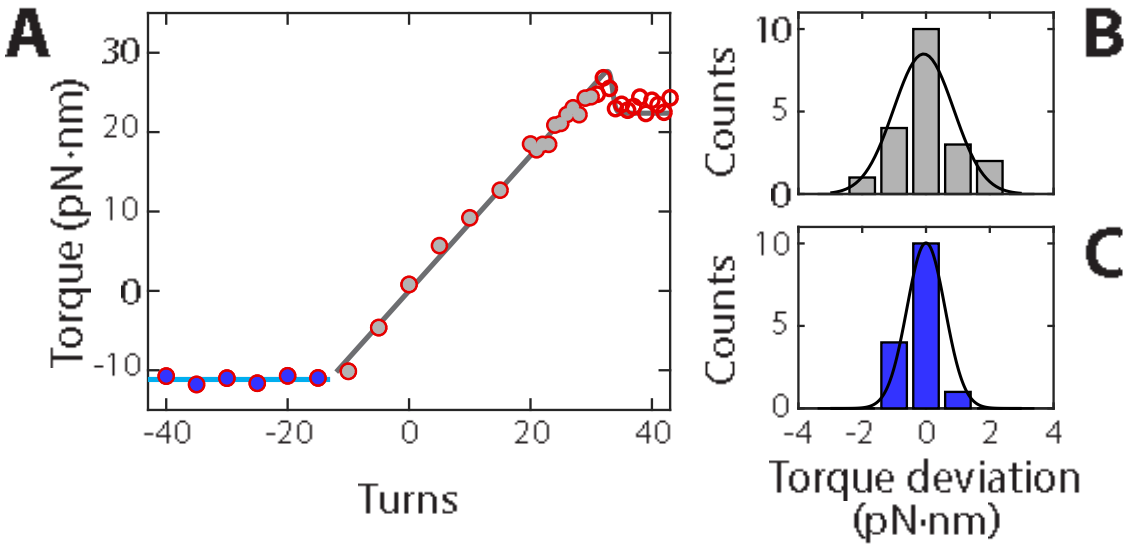

Figure S7. High-precision torque measurements in the eMTT and estimates of torque precision. A) Torque versus applied turns measurement for a 7.9 kbp DNA molecules in high-salt buffer (TE buffer with 550 mM NaCl) using 1.05 µm diameter MyOne beads at a stretching force of 3.5 pN, with an angular trap stiffness of ~50 pN·nm/rad). Data are taken from Figure 5d of Ref. (17). The experimental torque measurements are shown as red circles. Each data point corresponds to a measurement of 200 s. The solid dark gray line is a fit of a model of DNA elasticity (17). Data points in the elastic response regime of DNA (denoted in gray) are characterized by a linear torque versus turns dependence. At a negative torque of ~−11 pN·nm, DNA undergoes torque-induced melting (blue data points). **B)** Deviation of the experimental data in the linear response regime from the best linear fit (gray data points fitted by solid dark gray line in **A)**). The solid black line shows a Gaussian fit to the data, yielding a standard deviation of 0.9 pN·nm. **C)** Deviations of the experimental data in the torque-induced DNA melting regime from the best fit constant (blue data points fitted by solid light blue line in **A)**). The solid black line shows a Gaussian fit with a standard deviation of 0.6 pN·nm.

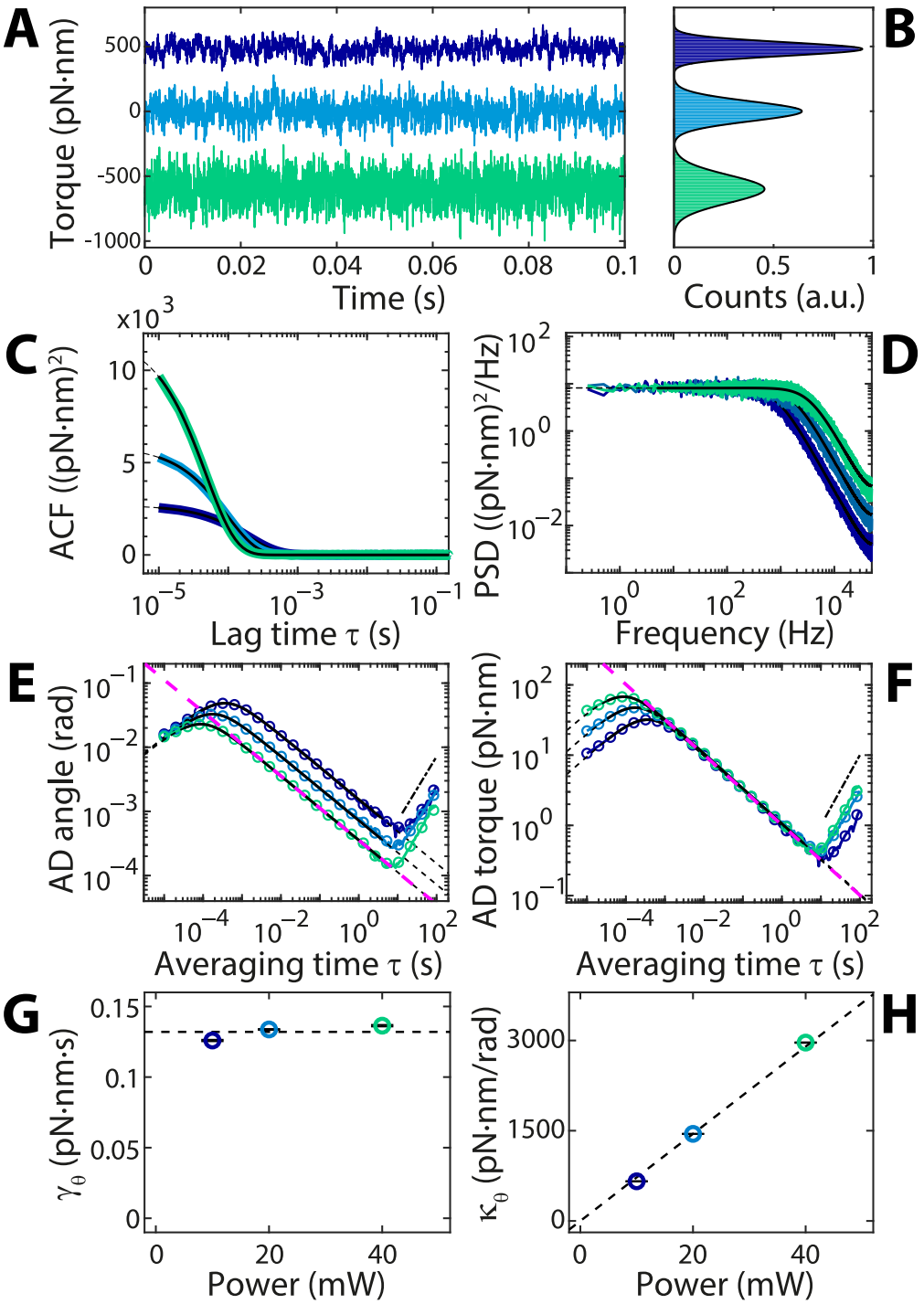

Figure S8. Additional analysis of the OTW data in Fig. 4 of the main text. The color-coding is the same as in the main text (10, 20, and 40 mW, going from dark blue to light green). **A)** Zoom-in on the first 0.1 s of the torque traces of 200 s each sampled at 100 kHz (corresponding to 2.0×10^7 data points). The traces are offset vertically for clarity. **B)** Histograms over the full traces. The solid black lines are Gaussian fits to the histograms. **C)** Autocorrelation function analysis. The solid black lines are fits to the data, and their extrapolations are shown as dashed black lines. **D)** Power spectrum analysis. **E)** Angle Allan deviation (AD). Colored lines (circles) reflect the normal AD (octave-sampled overlapping AD). Same data as in **Fig. 4B**. The dashed magenta line indicates the thermal limit for the stiffest trap. **F)** Torque AD. Same data as in **Fig. 4C**. The dashed magenta line corresponds to the thermal limit. The dash-dotted black line has slope $+1$, corresponding to linear drift. The fitted parameters are displayed in **G,H)**. **G)** Rotational drag coefficient γ_θ obtained from the torque AD fits in **F)** versus laser power. The dashed black line is a constant-value fit to the data. Same data as in **Fig. 4D**. The data points and their corresponding error bars denote the average and standard deviation, respectively, from $N = 5$ independent measurements**. H)** Rotational trap stiffness κ_θ obtained from the AD fits in **F)** versus laser power. The dashed black line is a linear fit to the data. Same data as in **Fig. 4E**.

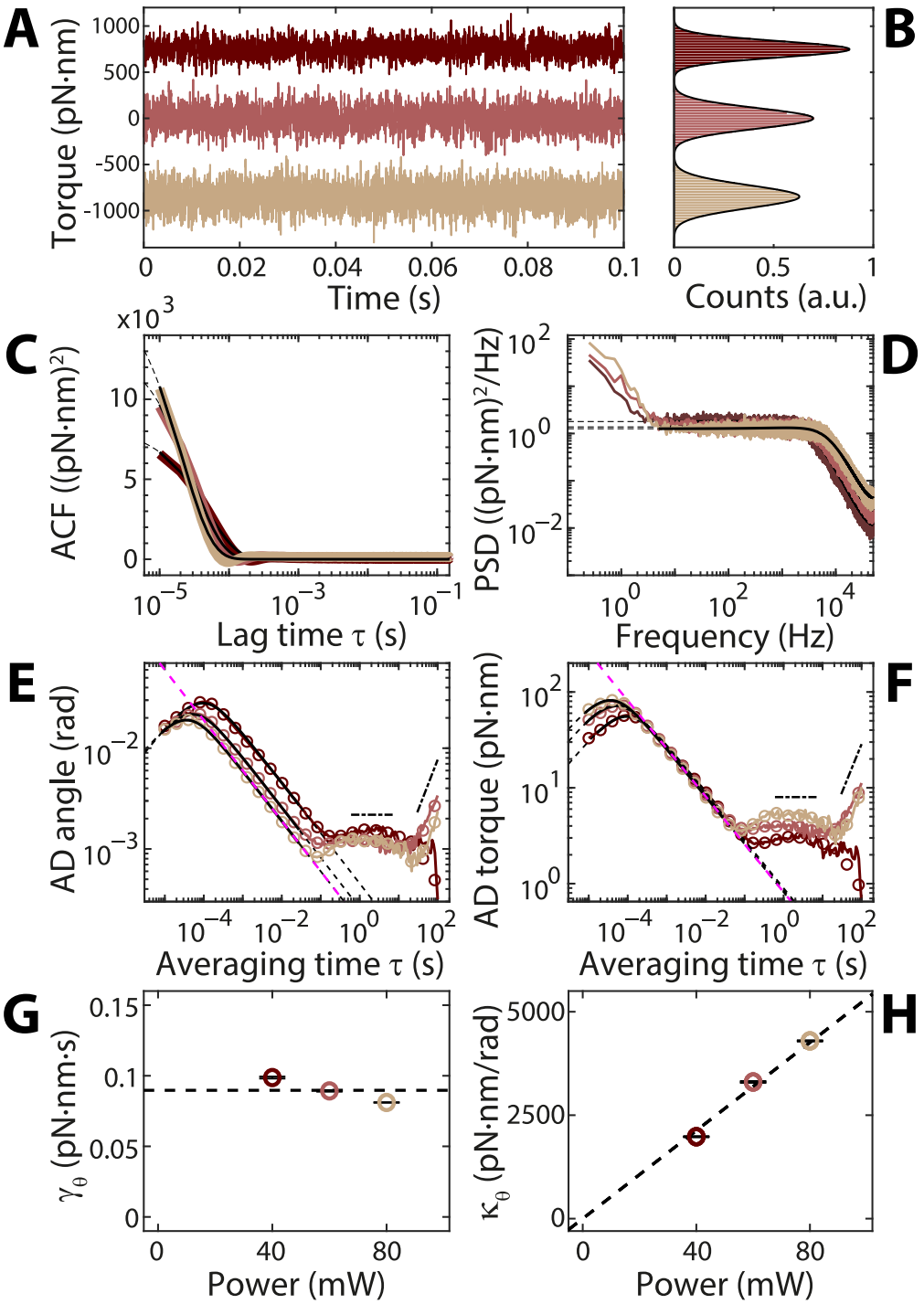

Figure S9. OTW data acquired under less favourable environmental conditions. The color-coding is as follows: 40, 60, and 80 mW, going from dark red-brown to light brown. **A)** Zoom-in on the first 0.1 s of the torque traces of 200 s each sampled at 100 kHz (corresponding to 2.0×10^7 data points). The traces are offset vertically for clarity. **B)** Histograms over the full traces. The solid black lines are Gaussian fits to the histograms. **C)** Autocorrelation function analysis. The solid black lines are fits to the data, and their extrapolations are shown as dashed black lines. **D)** Power spectrum analysis. **E)** Angle Allan deviation (AD). Colored lines (circles) reflect the normal AD (octave-sampled overlapping AD). The dashed magenta line indicates the thermal limit for the stiffest trap. **F)** Torque AD. The dashed magenta line corresponds to the thermal limit. Note the additional noise component (in contrast to **Fig. 4B,C** and **Supplementary Fig. S8E,F**) in the range 0.1–20 s, which we attribute to excess air currents present in the setup at the time of acquisition. The dash-dotted black lines have slope $+1$ or 0, corresponding to linear drift or $1/f$ noise, respectively. The fitted parameters are displayed in **G,H)**. **G)** Rotational drag coefficient γ_θ obtained from the torque AD fits in **F)** versus laser power. The dashed black line is a constant-value fit to the data. The data points and their corresponding error bars denote the average and standard deviation, respectively, from $N = 5$ independent measurements**. H)** Rotational trap stiffness κ_θ obtained from the AD fits in **F)** versus laser power. The dashed black line is a linear fit to the data.

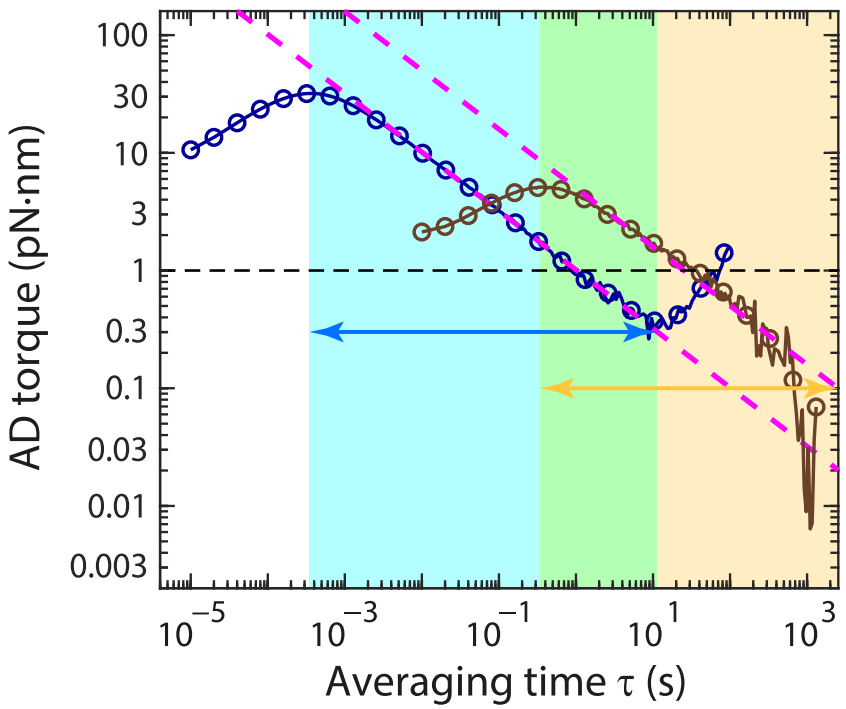

Figure S10. Comparison of the best achievable torque Allan deviation in the eMTT and OTW. The traces were selected from **Figs. 3C, 4C** to compare the best achievable torque precisions. We record the fluctuations of a MagSense bead (d = 0.7 μm) at 1 mT (dark brown) in eMTT, and a TiO_2 cylinder at 10 mW in OTW (dark blue). Colored lines (circles) reflect the normal AD (octave-sampled overlapping AD). The dashed magenta lines indicate the thermal limits. The color shading and the corresponding double-sided arrows indicate the averaging times (ranging from the timescale at which the Allan deviation peaks to that at which unwanted noise starts to dominate) over which the eMTT (light yellow) and the OTW (light blue) permit meaningful torque measurement. The range of averaging times in which the instruments' torque precision overlaps is shown in light green. The dashed black line corresponds to a torque precision of 1 pN·nm.

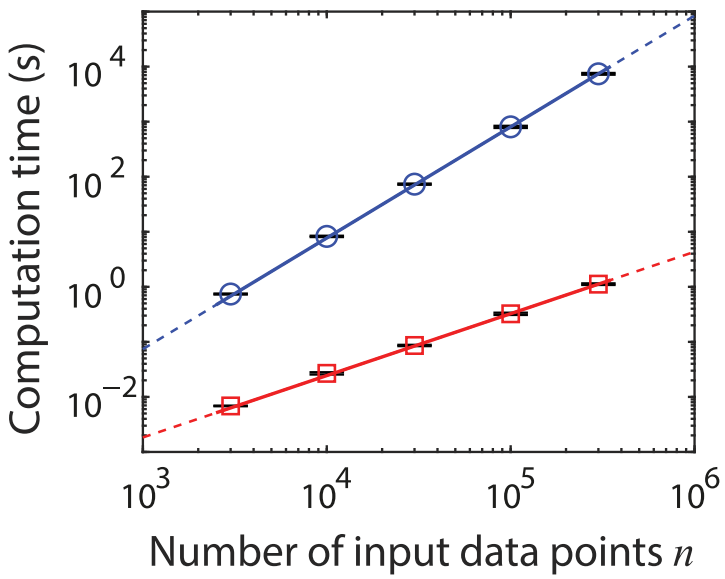

Figure S11. Comparison of efficiency in overlapping Allan variance computation. The overlapping Allan variance computation times as a function of the number of input data points n. The blue circles and red squares reflect the use of all available integration times $(m\tau_s;\ m = integer)$ and octave-sampled integration times $(m\tau_s;\ m = 2^{integer})$, respectively. The solid colored lines are power-law fits to the data, $computation\ time \propto n^{\alpha}$($\alpha = 2.0$ and 1.1 for blue circles and red rectangles, respectively), with their extrapolations shown as dashed colored lines. The data points and their corresponding error bars denote the average and standard deviation, respectively, for $N = 3$ computations.

Supplementary References

1. Czerwinski, F., A. C. Richardson, and L. B. Oddershede. 2009. Quantifying noise in optical tweezers by Allan variance. *Opt. Express.* 17:13255-13269.
2. Mahamdeh, M., and E. Schäffer. 2009. Optical tweezers with millikelvin precision of temperature-controlled objectives and base-pair resolution. *Opt. Express.* 17:17190-17199.
3. Andersson, M., F. Czerwinski, and L. B. Oddershede. 2011. Optimizing active and passive calibration of optical tweezers. *J. Opt.* 13:044020.
4. Perkins, T. T. 2014. Ångström-precision optical traps and applications. *Annu. Rev. Biophys.* 43:279-302.
5. Howe, D. A., D. W. Allan, and J. A. Barnes. 1981. Properties of signal sources and measurement methods. *In* Proceedings of the 35th Annual Symposium on Frequency Control (IEEE), pp. A1-A47.
6. Lansdorp, B. M., and O. A. Saleh. 2012. Power spectrum and Allan variance methods for calibrating single-molecule video-tracking instruments. *Rev. Sci. Instrum.* 83:025115.
7. Allan, D. W., M. A. Weiss, and J. L. Jespersen. 1991. A frequency-domain view of time-domain characterization of clocks and time and frequency distribution systems. *In* Proceedings of the 45th Annual Symposium on Frequency Control (IEEE), pp. 667-678.
8. van Oene, M. M., L. E. Dickinson, F. Pedaci, M. Kober, D. Dulin, J. Lipfert, and N. H. Dekker. 2015. Biological magnetometry: torque on superparamagnetic beads in magnetic fields. *Phys. Rev. Lett.* 114:218301.
9. Volpe, G., S. Gigan, and G. Volpe. 2013. Simulation of a Brownian particle in an optical trap. *Am. J. Phys.* 81:224-230.
10. Rutman, J. 1978. Characterization of phase and frequency instabilities in precision frequency sources: fifteen years of progress. *Proc. IEEE.* 66:1048-1075.
11. Wong, W. P., and K. Halvorsen. 2006. The effect of integration time on fluctuation measurements: calibrating an optical trap in the presence of motion blur. *Opt. Express.* 14:12517-12531.
12. Lebel, P., A. Basu, F. C. Oberstrass, E. M. Tretter, and Z. Bryant. 2014. Gold rotor bead tracking for high-speed measurements of DNA twist, torque and extension. *Nat. Methods.* 11:456-462.
13. Yasuda, R., H. Miyata, and K. Kinosita, Jr. 1996. Direct measurement of the torsional rigidity of single actin filaments. *J. Mol. Biol.* 263:227–236.
14. Neuman, K. C., and A. Nagy. 2008. Single-molecule force spectroscopy: optical tweezers, magnetic tweezers and atomic force microscopy. *Nat. Methods.* 5:491-505.
15. Lipfert, J., M. Wiggin, J. W. J. Kerssemakers, F. Pedaci, and N. H. Dekker. 2011. Freely orbiting magnetic tweezers to directly monitor changes in the twist of nucleic acids. *Nat. Commun.* 2:439.
16. Lipfert, J., M. Wiggin, J. W. J. Kerssemakers, F. Pedaci, and N. H. Dekker. 2015. Corrigendum: Freely orbiting magnetic tweezers to directly monitor changes in the twist of nucleic acids. *Nat. Commun.* 6:7192.
17. Janssen, X. J., J. Lipfert, T. Jager, R. Daudey, J. Beekman, and N. H. Dekker. 2012. Electromagnetic torque tweezers: a versatile approach for measurement of single-molecule twist and torque. *Nano Lett.* 12:3634-3639.